UNIVERSITY of CALIFORNIA
SANTA CRUZ

The Effects Of Rotation On Stratified Turbulence

A thesis submitted in partial satisfaction of the
requirements for the degree of

MASTER OF SCIENCE

in

SCIENTIFIC COMPUTING & APPLIED MATHEMATICS

by

Dante Buhl

September 2024

The thesis of Dante Buhl is approved:

Professor Pascale Garaud, Chair

Professor Nicholas Brummell

Professor Greg Chini

Peter F. Biehl
Vice Provost & Dean of Graduate Studies

Contents

List of Figures

Abstract

The Effects of Rotation on Stratified Turbulence

by

Dante Buhl

Recent interest in the dynamics of stratified turbulence has led to the development of new models for quantifying vertical transport of momentum and buoyancy (Chini et al 2022, Shah et al 2024). These models are still incomplete as they do not yet include all the relevant dynamics often present in real physical settings such as rotation and magnetic fields. Here we expand on prior work by adding rotation. Variation of the Rossby number affects the mean flow and perturbation dynamics independently. We conduct 3D direct numerical simulations of rotating, stochastically forced, strongly stratified turbulence ($Fr \ll 1$), and vary the Rossby number. We find that rotation gradually suppresses small-scale dynamics and, therefore, inhibits vertical transport as Ro decreases towards Fr. The effect is particularly pronounced within the cores of emergent cyclonic vortices. For sufficiently strong rotation, vertical motions are suppressed.

Dedications and Acknowledgements

This thesis is dedicated to all of those who have helped me get to where I am today. Including but not limited to my parents Guadalupe and John; my siblings Bella and Levi; my wonderful partner Isobel; and an amazingly supportive advisor Pascale Garaud.

I'd also like to acknowledge the Woods Hole Oceanographic Institute and the Geophysical Fluid Dynamics program there for allowing me to visit during the Summer of 2024 during which I was able to complete much of this thesis. I'd also like to acknowledge the Next Gen. Scholars in Applied Mathematics program, funded by an NSF S-STEM award, which has helped me through the beginning of graduate school in so many ways.

1 Introduction

Stratified Turbulence is a terminology introduced by D. K. Lilly to describe flows that exhibit three-dimensional anisotropic turbulence where vertical motions are limited due to stratification (Lilly, 1983). Stratification is defined to be the presence of a stable density profile $\bar{\rho}(z)$ whereby the density increases with depth ($d\bar{\rho}/dz < 0$). Displaced fluid parcels feel a restoring buoyancy force, which pulls them back toward equilibrium. The strength of the stratification is measured by its buoyancy frequency $N = \sqrt{-gd\ln(\bar{\rho})/dz}$ where g is the local gravity. Many geophysical and astrophysical systems have stratified regions, including the Earth's oceans and atmosphere and the radiative zones of stars and planets. The source of the stratification can either be temperature or composition (e.g. salinity in the oceans, helium content in stars).

Understanding stratified turbulence is vital to creating accurate models of the Earth's climate and of stellar interior dynamics, as it provides a mechanism for vertical mixing in an otherwise stable flow. In particular, purely diffusive dynamics are unable to explain the vertical transport of heat or momentum that is required to balance the global meridional overturning circulations in the oceans and atmosphere (Munk, 1966; Haynes et al., 1991). Similarly in stars, stratified turbulence is required to explain a large number of observations of chemical and angular momentum transport (Pinsonneault, 1997; Aerts et al., 2019).

Crucially, all of the aforementioned stratified turbulent flows take place in rotating bodies. The relevance of rotation for a given flow is described by the Rossby number Ro, commonly defined as

$$Ro = \frac{U}{2\Omega L} \ , \tag{1.1}$$

where U is the characteristic velocity of the flow, Ω is the angular velocity, and L is the characteristic length scale of the flow. On Earth, the rotation rate is roughly $7.3 \cdot 10^{-5} s^{-1}$ and common oceanic flows such as the Gulf Stream, which has a typical velocity of order $1 m/s$ and a length scale on the order of $100 km$ would have Rossby number $Ro = O(0.1)$. The Jet Stream on Earth has characteristic lengthscales of thousands of kilometers and a typical velocity of roughly $100 m/s$ implying that the Rossby number is $Ro = O(0.01)$. The Solar Tachcoline, a strongly stratified layer beneath the solar convective zone, has an estimated Rossby number $Ro = O(0.1)$ (Thompson et al., 1996). The effect of rotation becomes important as the

Rossby number decreases below $O(1)$ and so it is clear that many of these flows are rotationally influenced in addition to being stably stratified.

Recent theoretical work on the subject of stratified turbulence has improved our understanding of vertical mixing through the use of asymptotic analysis of governing equations (Chini et al., 2022; Shah et al., 2023) and high-resolution direct numerical simulations (Cope et al., 2020; Garaud, 2020; Garaud et al., 2024). The results of these studies have provided predictions for the various proxies for vertical transport. In particular, the vertical lengthscale of the turbulence is found to scale as U/N, which matches previously hypothesized scaling laws evinced by laboratory experiments (Park et al., 1994; Holford & Linden, 1999; Billant & Chomaz, 2000).

These results, however, have ignored the influence of rotation on stratified turbulence. Laboratory experiments of rotating stratified turbulence have demonstrated the importance of Ω/N as a control parameter. Praud et al. (2006) conducted experiments of decaying rotating stratified turbulence and showed that the eddies are elongated and vertically invariant when Ω/N is greater than 1. This suggests that U/N is no longer the relevant parameter in the limit of rapid rotation. Similarly, Aubert et al. (2012) showed that the aspect ratio for isolated vortices in rotating stratified flows depends on Ω/N.

In this thesis, we therefore attempt to understand the effect of rotation on previously developed models of stratified turbulence. In section 2, we present the model considered and governing equations. In section 3, we review the multiscale theory presented by Chini et al. (2022), and Shah et al. (2023), and DNS presented by Cope et al. (2020), Garaud (2020), and Garaud et al. (2024). In section 4, we run direct numerical simulations of stably stratified turbulence forced using stochastic Gaussian processes similar to the forcing mechanism used by Waite & Bartello (2004) and Waite & Bartello (2006) and compare it to the DNS in Garaud (2020) and Garaud et al. (2024). Finally, in section 5, we investigate the effect of rotation. We conduct DNS of rotating stratified turbulence in order to understand at what critical Rossby number the previously developed models become ineffective at describing the flow. In addition, we study the flow structures and mixing present when the flow becomes strongly influenced by rotation. Finally, we attempt to explain the DNS results by including rotation in the multiscale theory.

2 Model

2.1 Governing Equations

We begin with the Boussinesq equations for fluid motion in the presence of a stably stratified temperature field (with background temperature gradient $d\bar{T}/dz$) in a rotating coordinate system. The governing equations are

$$\frac{\partial \boldsymbol{u}}{\partial t} + \boldsymbol{u}\cdot\nabla\boldsymbol{u} + 2\boldsymbol{\Omega}\times\boldsymbol{u} = -\frac{1}{\rho_m}\nabla\tilde{p} + \alpha_T g\tilde{T}\boldsymbol{e}_z + \frac{1}{\rho_m}\boldsymbol{F} + \nu\nabla^2\boldsymbol{u}, \quad \text{Momentum Equation} \tag{2.1}$$

$$\frac{\partial \tilde{T}}{\partial t} + \boldsymbol{u}\cdot\nabla\tilde{T} + \frac{d\bar{T}}{dz}w = \kappa\nabla^2\tilde{T}, \quad \text{Temperature Equation} \tag{2.2}$$

$$\nabla\cdot\boldsymbol{u} = 0, \quad \text{Continuity Equation} \tag{2.3}$$

where $\mathbf{F}$ is a horizontal body force applied to drive the flow, and $\boldsymbol{\Omega}$ is the rotation rate, which is assumed to be aligned with the direction of gravity $\boldsymbol{g} = -g\boldsymbol{e}_z$. We denote the fluid velocity as $\boldsymbol{u} = \langle u, v, w\rangle$ and perturbations in pressure and temperature away from an assumed hydrostatic equilibrium as $\tilde{p}, \tilde{T}$ respectively. Other important quantities that arise here are the kinematic viscosity ν, the thermal diffusivity κ, the thermal expansion coefficient α_T, and the mean density ρ_m. These are assumed to be constants by the Boussinesq approximation.

Note the presence of the Coriolis force $2\boldsymbol{\Omega}\times\boldsymbol{u}$. This term is the essential distinguishing factor from prior work on this subject. Generally, $\boldsymbol{\Omega}$ is not aligned with gravity, and the angle between the rotation axis and gravity depends on the latitude. In order to reduce the complexity of the problem, in this thesis the effect of rotation will be studied only near the poles of rotating bodies where $\boldsymbol{e}_{\boldsymbol{\Omega}} \approx \boldsymbol{e}_z$.

Non-Dimensionalization

We non-dimensionalize the system using the following substitutions:

$$\boldsymbol{u} = U\hat{\boldsymbol{u}}, \quad \nabla = \frac{1}{L}\hat{\nabla},$$
$$\tilde{T} = L\frac{d\bar{T}}{dz}\hat{T}, \quad t = \frac{L}{U}\hat{t}, \quad \tilde{p} = \frac{U^2}{\rho_m}\hat{p},$$

where the unit velocity U is a characteristic horizontal velocity of the large-scale flow field, and the unit length L is a characteristic length scale of the horizontal forcing. The unit temperature is chosen to be the background temperature gradient multiplied by the length scale of the system. Finally, a unit timescale is obtained by the quotient of the unit length and velocity of the system. This quantity is effectively the turnover time of the large-scale horizontal eddies. Substituting these non-dimensional quantities into the governing equations we obtain:

$$\frac{\partial \hat{\boldsymbol{u}}}{\partial \hat{t}} + \hat{\boldsymbol{u}} \cdot \hat{\nabla} \hat{\boldsymbol{u}} + \frac{1}{Ro}(\boldsymbol{e_\Omega} \times \hat{\boldsymbol{u}}) = -\hat{\nabla}\hat{p} + \frac{1}{Fr^2}\hat{T}\boldsymbol{e}_z + \hat{\boldsymbol{F}} + \frac{1}{Re}\hat{\nabla}^2\hat{\boldsymbol{u}}, \tag{2.4}$$

$$\frac{\partial \hat{T}}{\partial \hat{t}} + \hat{\boldsymbol{u}} \cdot \hat{\nabla}\hat{T} + \hat{w} = \frac{1}{Pe}\hat{\nabla}^2\hat{T}, \tag{2.5}$$

$$\hat{\nabla} \cdot \hat{\boldsymbol{u}} = 0, \tag{2.6}$$

where $\boldsymbol{F} = (U^2\rho_m/L)\hat{\boldsymbol{F}}$ and the standard Rossby, Reynolds, Péclet and Froude numbers have appeared:

$$Ro = \frac{U}{2\Omega L}, \quad Re = \frac{UL}{\nu}, \quad Pe = \frac{UL}{\kappa},$$
$$Fr = \frac{U}{NL} = \frac{U}{\sqrt{\alpha_T g d\bar{T}/dz L}} \ .$$

These dimensionless quantities are indicators of the relevant dynamics of the flow. The Rossby number compares the rotation period of the flow to the large-scale horizontal eddy turnover time. The Reynolds number is the ratio of the viscous dissipation timescale across the eddy to the eddy turnover timescale. The Péclet number is the ratio of the thermal dissipation timescale across the eddy to the eddy turnover timescale. Finally, the Froude number is the ratio of the fastest gravity wave oscillation timescale to the large-scale eddy turnover timescale.

Hereafter, the hats are dropped for ease of notation.

2.2 Domain

In all that follows, we shall solve the governing equations inside of a tripply periodic domain with dimensions $L_x \times L_y \times L_z = 4\pi \times 4\pi \times \pi$. The domain can be seen in Figure 1. This domain has a square horizontal cross-section so that the flow obtained and the forcing used may be horizontally isotropic. It is shorter in the vertical to save computational time with the

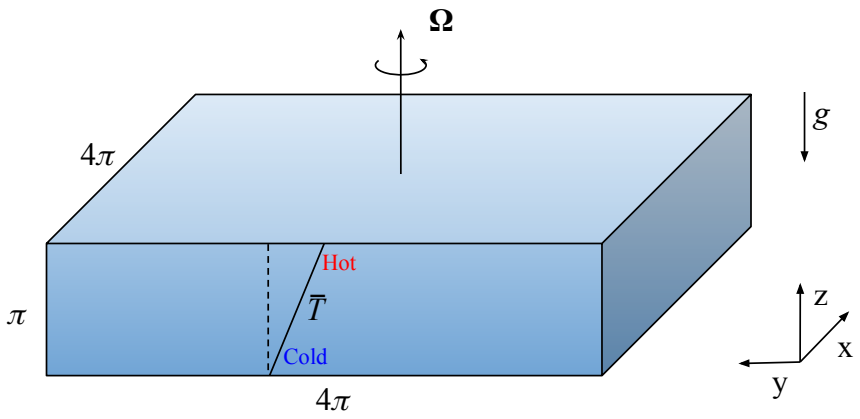

Figure 1: Schematic of the Domain

expectation that the vertical turbulent length scales are much shorter than the horizontal ones. We will also define a volume average operator $\langle\cdot\rangle$:

$$\langle q \rangle (t) = \frac{1}{L_x L_y L_z} \int_D q(\boldsymbol{x}, t) dV. \tag{2.7}$$

2.3 Energetics

Over long timescales, forced stratified turbulence reaches a stationary state where energy input by the body force balances viscous and thermal dissipation by the turbulent flow. To show this, we derive an energy equation by taking the dot product of the momentum equation (2.4) with $\boldsymbol{u}$, and multiplying the temperature equation (2.5) with T:

$$\boldsymbol{u} \cdot \frac{\partial \boldsymbol{u}}{\partial t} + \boldsymbol{u} \cdot (\boldsymbol{u} \cdot \nabla \boldsymbol{u}) + \boldsymbol{u} \cdot \frac{1}{Ro}(\boldsymbol{e}_z \times \boldsymbol{u}) = -\boldsymbol{u} \cdot \nabla p + \frac{w}{Fr^2} T + \boldsymbol{u} \cdot \boldsymbol{F} + \boldsymbol{u} \cdot \frac{1}{Re} \nabla^2 \boldsymbol{u}, \tag{2.8}$$

$$T \frac{\partial T}{\partial t} + T \boldsymbol{u} \cdot \nabla T + T w = \frac{1}{Pe} T \nabla^2 T. \tag{2.9}$$

We can simplify these equations by using the continuity equation to write them in conservative form

$$\frac{\partial E}{\partial t} + \nabla \cdot \left(\boldsymbol{u} E + \boldsymbol{u} p - \frac{1}{Re} \nabla E \right) = \frac{w}{Fr^2} T + \boldsymbol{u} \cdot \boldsymbol{F} - \frac{1}{Re} |\nabla \boldsymbol{u}|^2, \tag{2.10}$$

$$\frac{\partial P}{\partial t} + \nabla \cdot \left(\boldsymbol{u} P - \frac{1}{Pe} \nabla P \right) = -T w - \frac{1}{Pe} |\nabla T|^2, \tag{2.11}$$

where $E = \boldsymbol{u}^2/2$ and $P = T^2/2$. We then take the volume average of equations (2.10) and (2.11). Note that the divergence terms on the left-hand side integrate to zero in a triply periodic domain. Assuming the flow is in a statistically stationary state, i.e. $\frac{\partial \langle q \rangle}{\partial t} = 0$, then:

$$0 = \left\langle \frac{w}{Fr^2} T + \boldsymbol{u} \cdot \boldsymbol{F} - \frac{1}{Re} |\nabla \boldsymbol{u}|^2 \right\rangle, \tag{2.12}$$

$$0 = \left\langle -Tw - \frac{1}{Pe} |\nabla T|^2 \right\rangle. \tag{2.13}$$

We leverage the fact that the volume average is a linear operator and find that for the total energy to be conserved in a statistically steady state, the following balances must hold:

$$\langle \boldsymbol{u} \cdot \boldsymbol{F} \rangle = \frac{\chi}{Fr^2} + \epsilon_u, \tag{2.14}$$

$$\mathcal{B} = -\chi, \tag{2.15}$$

where $\mathcal{B}$ is the temperature flux, χ is the thermal dissipation rate and ϵ_u is the viscous dissipation rate, defined as

$$\mathcal{B} = \langle wT \rangle, \quad \chi = \frac{\langle |\nabla T|^2 \rangle}{Pe}, \quad \epsilon_u = \frac{\langle |\nabla \boldsymbol{u}|^2 \rangle}{Re} \ . \tag{2.16}$$

Both terms on the right-hand side of (2.14) act as a net sink in the energy equation since $\chi, \epsilon_u > 0$ by definition. The power input $\langle \boldsymbol{u} \cdot \boldsymbol{F} \rangle$ is therefore needed to balance the energy dissipation in the domain.

An important diagnostic quantity for vertical transport and mixing is the mixing efficiency η which we define here as:

$$\eta = \frac{\chi/Fr^2}{\chi/Fr^2 + \epsilon_u} = \frac{\chi/Fr^2}{\langle \boldsymbol{u} \cdot \boldsymbol{F} \rangle}. \tag{2.17}$$

This can be interpreted as the fraction of the kinetic energy input into the system that is irreversibly transferred into potential energy, and then lost via thermal dissipation.

2.4 Forcing Mechanism

Various studies of stratified turbulence have relied on several different forcing mechanisms. Some examples of forcing mechanisms are the sinusoidal shear forcing (Cope et al., 2020; Garaud

et al., 2024), vertical and streamwise shear forcings (Yi & Koseff, 2023), "vortical mode" forcing (Herring & Metais, 1989; Waite & Bartello, 2004, 2006; Brethouwer et al., 2007; Maffioli et al., 2016; Howland et al., 2020), and mean-relaxation forcing (Smith et al., 2021) among others. It has been shown by Howland et al. (2020) and Yi & Koseff (2023) that flows with different forcing mechanisms have different scaling laws for the mixing efficiency as a function of the input parameters. This is likely due to the fact that different types of instabilities are triggered in each case, which drive turbulent motions with different mixing properties.

For this thesis, we have chosen to use a "vortical mode" forcing inspired by Waite & Bartello (2004). We will force the horizontal vortical modes using horizontally-isotropic and divergence-free stochastic processes. By doing so, vertical flow and structure will arise indirectly and spontaneously from the dynamics and instabilities of the flow. We define our forcing as

$$\boldsymbol{F} = F_x \boldsymbol{e}_x + F_y \boldsymbol{e}_y, \quad \nabla \cdot \boldsymbol{F} = 0. \tag{2.18}$$

As the governing equations will be solved using pseudospectral Direct Numerical Simulations (DNS), the forcing will be applied in spectral space. Specifically, we express the forcing in Fourier spectral space

$$\hat{\boldsymbol{F}}(\boldsymbol{k}, t) = \hat{F}_x(\boldsymbol{k}, t)\boldsymbol{e}_x + \hat{F}_y(\boldsymbol{k}, t)\boldsymbol{e}_y, \tag{2.19}$$

$$\hat{F}_x = \frac{k_y}{|\boldsymbol{k_h}|} G(\boldsymbol{k}, t), \quad \hat{F}_y = \frac{-k_x}{|\boldsymbol{k_h}|} G(\boldsymbol{k}, t), \tag{2.20}$$

where $G(\boldsymbol{k}, t)$ is a time-dependent Gaussian process and $\hat{\boldsymbol{F}}$ denotes the Fourier transform of $\boldsymbol{F}$. This configuration ensures that $\boldsymbol{k} \cdot \hat{\boldsymbol{F}} = 0$. Unlike Alvelius (1999), Lindborg (2006), we use no amplitude function or adaptive scaling to ensure that the power input is constant at each timestep. Rather, we rely on the power input being in a statistically stationary state. For the simulations presented later, we only force horizontal wavenumbers $\boldsymbol{k}_h \leq \sqrt{2}$, to ensure that the largest horizontal scales are $O(1)$ as implied by our non-dimensionalization.

2.5 Gaussian Processes

Gaussian Processes are stochastic processes specified by their mean function $\mu(t)$ and covariance function $K(t, t')$ (Williams & Rasmussen, 1995). To build a regression $\boldsymbol{G}$, Gaussian processes

sample from a joint multivariate Gaussian distribution centered on the training set $(\boldsymbol{t}, \boldsymbol{y})$

$$\boldsymbol{G} \sim \mathcal{N}(\boldsymbol{\mu}_*, \boldsymbol{\Sigma}), \tag{2.21}$$

where $\boldsymbol{\mu}_*$ is the mean vector of the distribution and $\boldsymbol{\Sigma}$ is the covariance matrix generated using the covariance function. There are many valid covariance functions suited for various purposes. For this thesis, we consider Gaussian processes with mean $\mu(t) = 0$ and covariance function defined by the exponential squared kernel

$$K(t, t') = \exp\left(\frac{-(t - t')^2}{2\tau^2}\right), \tag{2.22}$$

where τ is the correlation parameter of the Gaussian process. The correlation parameter affects the timescale of the regression generated, e.g. $\tau \ll 1$ would generate a high-frequency regression. We use $\tau = 0.2$ and a constant timestep of $\Delta t = 0.05$. We define $\boldsymbol{\mu}_*$ and $\boldsymbol{\Sigma}$ for a sample set $\boldsymbol{t}'$:

$$\boldsymbol{\mu}_* = \mathbf{K}'^T \mathbf{K}^{-1} \boldsymbol{y}, \tag{2.23}$$

$$\boldsymbol{\Sigma} = \mathbf{K}'' - \mathbf{K}'^T \mathbf{K}^{-1} \mathbf{K}', \tag{2.24}$$

where $[\mathbf{K}]_{ij} := K(\boldsymbol{t}_i, \boldsymbol{t}_j)$, $[\mathbf{K}']_{ij} := K(\boldsymbol{t}_i, \boldsymbol{t}'_j)$, and $[\mathbf{K}'']_{ij} := K(\boldsymbol{t}'_i, \boldsymbol{t}'_j)$. This versatile process can be applied to any number of training points n with a standard operation cost of $O(n^3)$ due to the matrix inversion $\mathbf{K}^{-1}$.

In practice, the Gaussian Process procedure for generating a time series needs to be modified to improve the condition number of the matrix $\mathbf{K}$. Indeed, equations (2.23) and (2.24) use the inverse of $\mathbf{K}$ in order to generate a time series, and this matrix is prone to having a large condition number. In order to control the conditioning of this matrix and improve the numerical stability of this process, we employ the pseudo-inverse $\mathbf{K}_p^{-1}$ defined as

$$\mathbf{K}_p^{-1} := \boldsymbol{V}_p \boldsymbol{D}_p^{-1} \boldsymbol{V}_p^T, \tag{2.25}$$

$$\boldsymbol{D}_p := \text{diag}(\lambda_1, \cdots, \lambda_c), \quad |\lambda_c| > \epsilon |\lambda_1|, \tag{2.26}$$

$$\boldsymbol{V}_p := [\boldsymbol{\Lambda_1}, \cdots, \boldsymbol{\Lambda_c},] \tag{2.27}$$

where $(\lambda_i, \boldsymbol{\Lambda}_i)$ are corresponding eigenvalue-eigenvector pairs of $\mathbf{K}$ such that $|\lambda_i| \geq |\lambda_{i+1}|$, and

λ_c is the smallest eigenvalue such that $|\lambda_c| \geq \epsilon|\lambda_1|$. Here, ϵ is a controlled tolerance value for the condition number which we fix to be $\epsilon = 10^{-4}$. The definition of μ_* and $\mathbf{\Sigma}$ are adjusted to include the pseudo-inverse of $\mathbf{K}$:

$$\boldsymbol{\mu}_* = (\boldsymbol{V}_p^T \mathbf{K}')^T \boldsymbol{D}_p^{-1} (\boldsymbol{V}_p^T \boldsymbol{y}), \tag{2.28}$$

$$\mathbf{\Sigma} = \mathbf{K}'' - (\boldsymbol{V}_p^T \mathbf{K}')^T \boldsymbol{D}_p^{-1} (\boldsymbol{V}_p^T \mathbf{K}'). \tag{2.29}$$

Finally, since PADDI is implemented in Fortran 90, which lacks an intrinsic multivariate Gaussian distribution sampling function, we instead use the Box-Muller transform to generate a multivariate normal distribution of mean $\boldsymbol{\mu}_* = 0$ and $\mathbf{\Sigma} = \mathbf{I}$. This distribution is linearly transformed to have the mean and covariance desired. The Gaussian process (2.21) is modified to become:

$$\boldsymbol{G} = \boldsymbol{\mu}_* + \boldsymbol{M}\mathcal{N}(\mathbf{0}, \mathbf{I}), \tag{2.30}$$

where $\boldsymbol{M} = \boldsymbol{V}\boldsymbol{D}^{1/2}$ and $\boldsymbol{V}, \boldsymbol{D}$ are produced from the eigendecomposition of $\mathbf{\Sigma}$. The numerical implementation of the forcing mechanism presented in §2.4 relies on a linear interpolation of time series generated by a Gaussian process. This forcing mechanism produces complex-valued time series as seen in Figure 2, which is then used in (2.20) to produce the desired forcing.

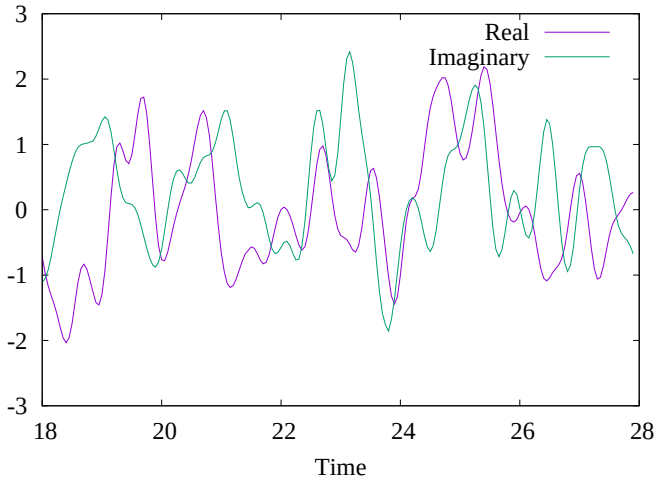

Figure 2: A portion of a time series generated by a Gaussian process used in one of the DNS. Its real and imaginary components are seen to vary randomly, with a mean value of 0 and an average amplitude of 1 on a $O(1)$ time scale.

3 Recent Work on Nonrotating Stratified Turbulence

In this section, we review a series of papers linking theoretically derived scaling laws to observations from direct numerical simulations, that have shown a great deal of success in advancing the field.

3.1 Multiscale Model of Stratified Turbulence

Chini et al. (2022) and Shah et al. (2023) obtained scaling laws for several transport properties of strongly stratified turbulence by performing a multiscale expansion of the governing equations. This is motivated by the notion that the turbulence contains a combination of large and small horizontal scales where the large scales are dominated by vortical "pancake" structures. The large-scale flows are, therefore, strongly anisotropic, with scales of order unity (by construction) in the horizontal direction, and scales of order α (with $\alpha \ll 1$) in the vertical direction. DNS results from Maffioli & Davidson (2016), Cope et al. (2020), Garaud (2020) further revealed that between these 'pancakes' there appeared to be eddies with a much smaller horizontal length scale. In order to capture the dynamics at both scales, Chini et al. (2022) developed a multiscale model with a small horizontal length scale of order α and a large horizontal length scale of $O(1)$. Crucially, they assume there is a single vertical scale of the same order as the small horizontal scale, implying isotropy on the small scales. Due to the faster turnover time of the smaller eddies, a new fast timescale is also introduced, associated with the shearing rate $1/\alpha$ between the 'pancake' eddies. Overall, we have:

$$\boldsymbol{x}_s = \boldsymbol{x}_h, \quad \boldsymbol{x}_f = \boldsymbol{x}_h/\alpha, \quad \zeta = z/\alpha, \quad t_s = t, \quad t_f = t/\alpha, \tag{3.1}$$

where the subscript s corresponds to large/slow scales and the subscript f corresponds to small/fast scales. Using the proposed rescaling of the coordinate system, the derivatives become

$$\nabla_h q = \nabla_s q + \frac{1}{\alpha}\nabla_f q, \quad \frac{\partial q}{\partial z} = \frac{1}{\alpha}\frac{\partial q}{\partial \zeta}, \quad \frac{\partial q}{\partial t} = \frac{\partial q}{\partial t_s} + \frac{1}{\alpha}\frac{\partial q}{\partial t_f}. \tag{3.2}$$

In addition to this multi-scale model for the flow, Chini et al. (2022) proposed to split each

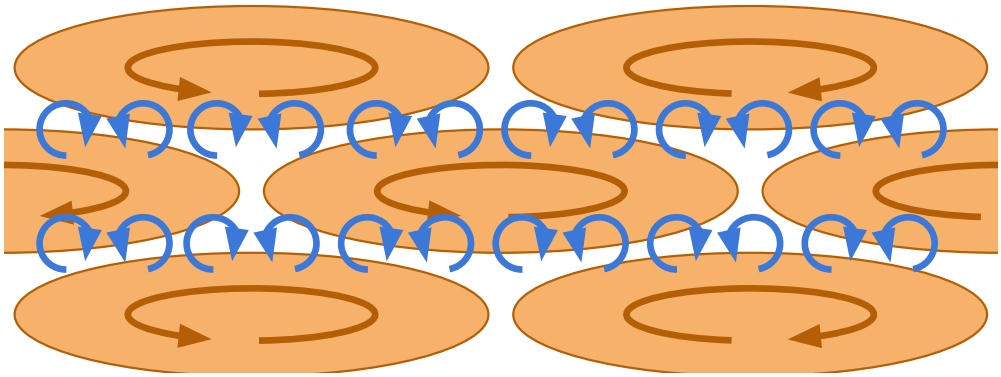

Figure 3: Multiscale eddy schematic. Larger, horizontally anisotropic eddies are seen in orange in counter-rotating pairs. Smaller, isotropic eddies are seen in blue.

quantity into a mean component $\bar{q}$ which varies on the larger/slower scales, and a perturbation component q' which varies on both the large/slow and small/fast scales:

$$q(\boldsymbol{x}_h, \zeta, t) = \bar{q}(\boldsymbol{x}_s, \zeta, t_s) + q'(\boldsymbol{x}_s, \boldsymbol{x}_f, \zeta, t_s, t_f). \tag{3.3}$$

A fast-averaging operator is also defined to isolate mean and perturbation dynamics:

$$\overline{q}(\boldsymbol{x}_s, \zeta, t_s) \equiv \lim_{\tau_f, l_x, l_y \to \infty} \frac{1}{l_x l_y \tau_f} \int_0^{\tau_f} \int_{\boldsymbol{D}_h} q(\boldsymbol{x}_s, \boldsymbol{x}_f, \zeta, t_s, t_f) d\boldsymbol{x}_f dt_f. \tag{3.4}$$

An important property of the mean-perturbation representation is that perturbations fast-average to zero ($\overline{q'} = 0$), while mean quantities are unaffected ($\overline{\bar{q}} = \bar{q}$).

Non-diffusive Dynamics

Chini et al. (2022) applied this multiscale model to the governing equations for stratified turbulence in the following asymptotic limit ($Fr \ll 1, Re \gg 1, Pe \gg 1$), such that the so-called buoyancy Renolds number defined as $Re_b = \alpha^2 Re$, and the buoyancy Péclet number defined as $Pe_b = \alpha^2 Pe$ are both of order unity or larger. The governing equations are split into mean-perturbation form and multiscale derivatives are substituted into derivative operators. The averaging operator defined in (3.4) is used to produce the mean equations, which are then subtracted from the total equations to obtain the perturbation equations. Applying this to the

continuity equation (2.6), they find:

$$\nabla_s \cdot \bar{\boldsymbol{u}}_h + \frac{1}{\alpha}\frac{\partial \bar{w}}{\partial \zeta} = 0, \tag{3.5}$$

$$\frac{1}{\alpha}\nabla_f \cdot \boldsymbol{u}'_h + \frac{1}{\alpha}\frac{\partial w'}{\partial \zeta} + h.o.t. = 0. \tag{3.6}$$

Chini et al. (2022) noted that $\bar{w} = O(\alpha)$ must hold in order for the mean flow to remain fully three-dimensional. At the leading order, the perturbation equation reveals that the horizontal perturbations are of the same order as the vertical perturbations, i.e., $\boldsymbol{u}'_h = O(w') = O(\boldsymbol{u}')$.

A similar procedure is applied to the horizontal component of the momentum equation and gives:

$$\frac{\partial \bar{\boldsymbol{u}}_h}{\partial t_s} + \bar{\boldsymbol{u}}_h \cdot \nabla_s \bar{\boldsymbol{u}}_h + \frac{1}{\alpha}\overline{\boldsymbol{u}'_h \cdot \nabla_f \boldsymbol{u}'_h} + \frac{\bar{w}}{\alpha}\frac{\partial \bar{\boldsymbol{u}}_h}{\partial \zeta} + \overline{\frac{w'}{\alpha}\frac{\partial \boldsymbol{u}'_h}{\partial \zeta}} = -\nabla_s \bar{p} + \bar{\boldsymbol{F}}_h + \frac{1}{Re_b}\frac{\partial^2 \bar{\boldsymbol{u}}_h}{\partial \zeta^2} + h.o.t., \tag{3.7}$$

$$\frac{1}{\alpha}\frac{\partial \boldsymbol{u}'_h}{\partial t_f} + \frac{1}{\alpha}\bar{\boldsymbol{u}}_h \cdot \nabla_f \boldsymbol{u}'_h + \frac{w'}{\alpha}\frac{\partial \bar{\boldsymbol{u}}_h}{\partial \zeta} = -\frac{1}{\alpha}\nabla_f p' + \frac{1}{Re_b}\left(\nabla_f^2 \boldsymbol{u}'_h + \frac{\partial^2 \boldsymbol{u}'_h}{\partial \zeta^2}\right) + h.o.t.. \tag{3.8}$$

This reveals the buoyancy Reynolds number defined above to be the effective Reynolds number of the large-scale 'pancake' eddies due to their shorter vertical extent. They noted that for the fast-averaged Reynolds stresses to affect the mean dynamics at leading order requires $\boldsymbol{u}' = O(\alpha^{1/2})$. We also see that the effective Reynolds number of the perturbations is larger, namely Re_b/α, due to their faster turnover time.

A similar decomposition yields the mean and perturbation equations for $\bar{T}$ and T' respectively:

$$\frac{\partial \bar{T}}{\partial t_s} + \bar{\boldsymbol{u}}_h \cdot \nabla_s \bar{T} + \frac{1}{\alpha}\overline{\boldsymbol{u}'_h \cdot \nabla_f T'} + \frac{1}{\alpha}\bar{w}\frac{\partial \bar{T}}{\partial \zeta} + \frac{1}{\alpha}\overline{w'\frac{\partial T'}{\partial \zeta}} + \bar{w} = \frac{1}{Pe_b}\frac{\partial^2 \bar{T}}{\partial \zeta^2} + h.o.t., \tag{3.9}$$

$$\frac{1}{\alpha}\frac{\partial T'}{\partial t_f} + \frac{1}{\alpha}\bar{\boldsymbol{u}}_h \cdot \nabla_f T' + \frac{w'}{\alpha}\frac{\partial \bar{T}}{\partial \zeta} + w' = \frac{1}{Pe_b}\left(\nabla_f^2 T' + \frac{\partial^2 T'}{\partial \zeta^2}\right) + h.o.t.\ . \tag{3.10}$$

Similar to the momentum equations, Chini et al. (2022) observed that the relevant temperature diffusion parameter is $Pe_b = \alpha^2 Pe$ in the mean equation, and Pe_b/α in the perturbation equation. The following result is predicated on the assumption that $Pe_b \geq O(1)$. As the vertical advection of the background temperature gradient is a crucial element of stratified turbulence, Chini et al. (2022) inferred that it must be of the same order as the horizontal advection terms,

leading to the conclusion that $\bar{T} = O(\bar{w})$, and similarly for the perturbations that $T' = O(\alpha w')$.

The mean and perturbation components of the vertical momentum equation are:

$$0 = -\frac{1}{\alpha}\frac{\partial \bar{p}}{\partial \zeta} + \frac{1}{Fr^2}\bar{T} + h.o.t., \tag{3.11}$$

$$\frac{1}{\alpha}\frac{\partial w'}{\partial t_f} + \frac{1}{\alpha}\bar{\boldsymbol{u}}_h \cdot \nabla_f w' = -\frac{1}{\alpha}\frac{\partial p'}{\partial \zeta} + \frac{1}{Fr^2}T' + \frac{1}{Re_b}\left(\nabla_f^2 w' + \frac{\partial^2 w'}{\partial \zeta^2}\right) + h.o.t.\ . \tag{3.12}$$

The mean equation at the leading order is revealed to be governed by hydrostatic balance and, furthermore, shows that $\alpha = Fr$. This result can be used to compute scaling laws for each variable as a function of the Froude number of the flow, including the mean vertical velocity $\bar{w} = O(Fr)$, the perturbation velocity $\boldsymbol{u}' = O(Fr^{1/2})$, the temperature fluctuation $T' = O(Fr^{3/2})$, the temperature flux $w'T' = O(Fr^2)$, and the vertical turbulent viscosity $w'l_z = O(Fr^{3/2})$. This implies, as expected, that as the stratification becomes stronger, vertical transport becomes inhibited.

Thermally Diffusive Dynamics

As mentioned before, the analysis of Chini et al. (2022) assumes that $Pe_b \geq O(1)$ which is always satisfied when $Re_b \geq O(1)$ and $Pr \geq O(1)$. If $Pr \ll 1$, however, this does not have to be the case and allows for new thermally diffusive regimes of stratified turbulence where $Re_b \geq O(1)$ but $Pe_b \ll 1$. Shah et al. (2023) recently extended the multiscale theory developed in Chini et al. (2022) for such low Prandtl number flows.

Taking the limit $Pe_b \ll 1$ does not directly affect the leading orders of the continuity or horizontal momentum equations. Several scaling laws obtained by Chini et al. (2022) therefore remain valid in this regime; i.e. we have $\bar{w} = O(\alpha)$, $\boldsymbol{u}' = O(\alpha^{1/2})$, $\bar{p} = O(1)$, and $p' = O(\alpha^{1/2})$. By contrast, taking $Pe_b \ll 1$ directly impacts the mean and fluctuation equations for the temperature, as shown by Shah et al. (2023), who identified two distinct regimes.

The first case is the intermittent regime: $\alpha \ll Pe_b \ll O(1)$. In this case, inspection of the temperature equations (3.9) and (3.10) shows that the leading order of the mean dynamics becomes significantly influenced by temperature diffusion while the perturbation dynamics remain

unaffected. Dominant balance in each equation implies

$$\bar{w} = \frac{1}{Pe_b}\frac{\partial^2 \bar{T}}{\partial \zeta^2} + h.o.t., \tag{3.13}$$

$$\frac{1}{\alpha}\frac{\partial T'}{\partial t_f} + \frac{1}{\alpha}\bar{\boldsymbol{u}}_h \cdot \nabla_f T' + \frac{w'}{\alpha}\frac{\partial \bar{T}}{\partial \zeta} + w' = \frac{1}{Pe_b}\left(\nabla_f^2 T' + \frac{\partial^2 T'}{\partial \zeta^2}\right) + h.o.t.\ . \tag{3.14}$$

The scaling of $\bar{T}$ needs to be chosen to ensure balance in the mean temperature equation (3.13) between the vertical advection of the background stratification and the diffusion of $\bar{T}$. This reveals that $\bar{T} = O(\alpha Pe_b)$. Shah et al. (2023) noted that in this limit, there are two choices of how to balance the vertical momentum equation. The first choice is to impose hydrostatic balance in the mean equation producing the scaling of $\alpha = Fr/\sqrt{Pe_b}$. Upon inspection of the perturbation equations, the temperature equation implies that $T' = O(\alpha^{3/2})$, but this reveals an inconsistency in the vertical momentum perturbation equation (3.12) where $T'/Fr^2 = O(\alpha^{-1/2}/Pe_b)$ is unbalanced. Shah et al. (2023) determined that hydrostatic balance must be imposed in the perturbation equations instead which recovers $\alpha = Fr$.

As a result, the scaling of $\bar{w}$, $\boldsymbol{u}'$ and T' retain their original dependence on Fr as in the non-diffusive regime, but the scaling of the mean temperature changes to be $\bar{T} = O(Fr^3 Pe)$. This regime was determined to be valid when $Re_b \geq O(1)$ and while $\alpha \ll Pe_b \ll 1$ which is equivalent to $Re \geq Fr^{-2}$ and $Fr^{-1} \ll Pe \ll Fr^{-2}$.

The next case is the fully diffusive regime where $Pe_b \ll \alpha$. In this case, thermal diffusion dominates the leading order of both the mean and perturbation dynamics. The temperature equations become:

$$\bar{w} = \frac{1}{Pe_b}\frac{\partial^2 \bar{T}}{\partial \zeta^2} + h.o.t., \tag{3.15}$$

$$w' = \frac{1}{Pe_b}\left(\nabla_f^2 T' + \frac{\partial^2 T'}{\partial \zeta^2}\right) + h.o.t., \tag{3.16}$$

which implies $\bar{T} = O(\alpha Pe_b)$ and $T' = O(\alpha^{1/2} Pe_b)$. Shah et al. (2023) notes that there are two choices to balance the vertical momentum equations. Similar to the intermittent regime, choosing to balance the mean equation first leads to an inconsistency in the perturbation equations. Thus Shah et al. (2023) balances the perturbation equation revealing $\alpha = Fr^2/Pe_b = \left(\frac{Fr^2}{Pe}\right)^{1/3}$ This value of α produces new scalings laws for the velocity and temperature, namely: $\bar{w} = O((Fr^2/Pe)^{1/3})$, $\boldsymbol{u}' = O((Fr^2/Pe)^{1/6})$, $\bar{T} = O(Fr^2)$, $T' = O(Fr^{5/3} Pe^{1/6})$, and predicts

that the vertical length scale of the turbulent eddies ought to be $O((Fr^2/Pe)^{1/3})$.

3.2 Numerical Results

Direct Numerical Simulations (DNS) by Cope et al. (2020) and Garaud et al. (2024) successfully validated the multiscale asymptotics of Chini et al. (2022) and Shah et al. (2023). These DNS were performed using the PADDI code, developed by Stephan Stellmach and described in Traxler et al. (2011). PADDI is a three-dimensional pseudospectral code that can solve equations (2.4) - (2.6) in a triply periodic domain. PADDI utilizes a pencil-based fast Fourier transform algorithm and a semi-implicit, three-step Adams-Bashforth method with adaptive time-stepping.

The majority of the simulations reported by Cope et al. (2020) and Garaud et al. (2024) used a domain size of $L_x = 4\pi$, $L_y = L_z = 2\pi$ with a steady horizontal shear forcing defined as $\boldsymbol{F} = \sin(y)\boldsymbol{e}_x$. They conducted simulations over a broad parameter space by varying the Froude number for different values of the Prandtl number thus spanning both the fully diffusive and non-diffusive regime. Characteristic results are shown in Figure 4, taken from Cope et al. (2020). The large anisotropic flow structures are most visible in the streamwise velocity component, and we see that layering dominates the flow in the stratified regimes. Small isotropic scales are clearly visible in the vertical component of the velocity field.

Cope et al. (2020) conducted simulations with $Pe \leq O(1)$, which guarantees that $Pe_b \ll O(\alpha)$ and therefore lies in the thermally diffusive regime found in Shah et al. (2023). They measured the vertical eddy length scale of the flow by using an autocorrelation function A_w defined as

$$A_w(l,t) = \frac{1}{L_x L_y L_z} \int w(x,y,z,t) w(x,y,z+l,t) dx dy dz, \tag{3.17}$$

and proposed to use the first zero of A_w as an estimate of the length scale l_z of the small-scale eddies. Cope et al. (2020) empirically obtained the same scaling law for $l_z = O((Fr^2/Pe)^{1/3})$ predicted in the thermally-diffusive limit by Shah et al. (2023). This is demonstrated in Figure 5. The figure also shows that the vertical rms velocity follows the predicted scaling of $\alpha^{-1/2} = (Fr^2/Pe)^{1/6}$ in the stratified turbulent regime.

Garaud (2020) performed DNS of stratified turbulence at $Pr = 0.1$, in a regime that Shah et al. (2023) later discovered to be the non-diffusive and intermediate stratified turbulence regimes. Her results are not as clear as those of Cope et al. (2020) and suggested an alternative

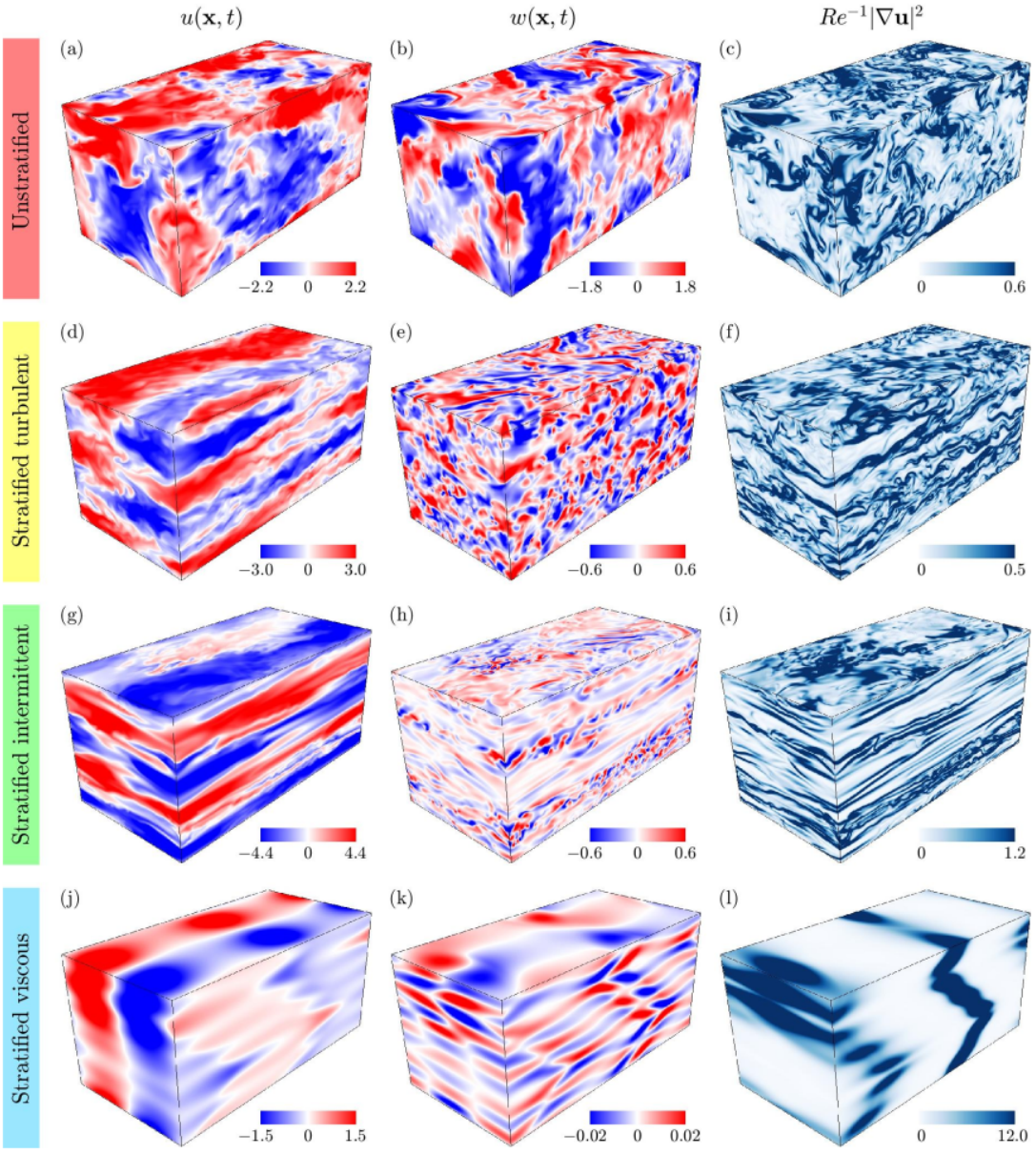

Figure 4: A diagram of the flow structures present in stratified flow simulations taken from Cope et al. (2020).

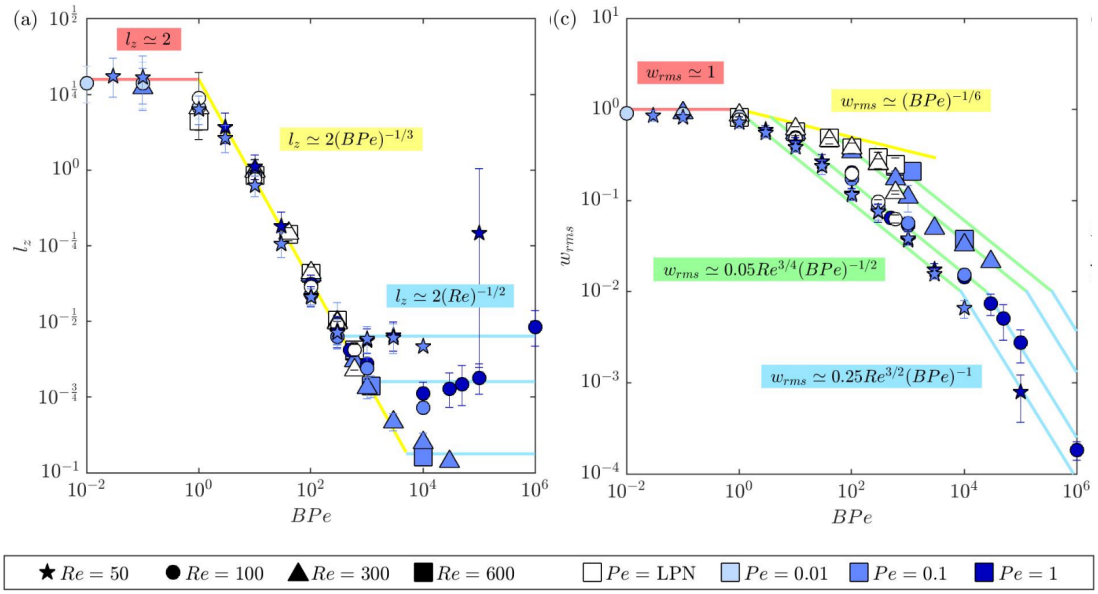

Figure 5: Plot of the vertical eddy length scale l_z (left) and mean vertical velocity $\bar{w}$ (right) taken Cope et al. (2020). The vertical eddy length scale decays proportional to $(BPe)^{-1/3} = (Fr^2/Pe)^{1/3}$ within the stratified turbulent regime (yellow).

scaling law where both $w_{\rm rms}$ and l_z scale as $Fr^{2/3}$, which does not fit the Chini et al. (2022) theory. In order to understand the origin of this unusual scaling law, Garaud et al. (2024) hypothesized that this could be related to the spatially intermittent nature of the turbulence, where large regions of the flow become increasingly laminar as the stratification increases. The multiscale analysis and derived scaling laws summarized in the previous section, by contrast, rely on the existence of small-scale turbulence. Garaud et al. (2024) proposed to numerically separate mean and perturbation dynamics by utilizing a vorticity weighting algorithm to separately measure the rms vertical velocity both inside and outside turbulence patches of the flow:

$$w_{\rm turb}(t) = \sqrt{\frac{\langle w^2\omega_z^2\rangle}{\langle\omega_z^2\rangle}} \text{ to estimate } w'_{\rm rms}, \tag{3.18}$$

$$w_{\rm lam}(t) = \sqrt{\frac{\langle w^2\omega_z^{-2}\rangle}{\langle\omega_z^{-2}\rangle}} \text{ to estimate } \bar{w}_{\rm rms}. \tag{3.19}$$

Using this algorithm, they found that $w_{\rm turb} \propto Fr^{1/2}$ while $w_{\rm lam} \propto Fr$, as predicted by Chini et al. (2022), see Figure 6.

As a result of these DNS and multiscale models, we now have a better understanding of the

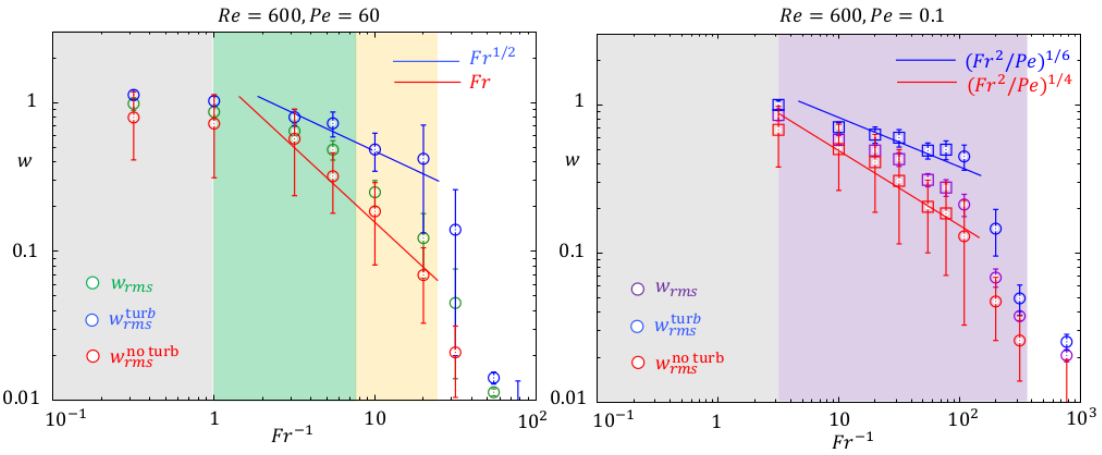

Figure 6: Plot of the weighted $w_{\rm rms}$ scaling from Garaud et al. (2024). Perturbation dynamics are plotted in blue and mean dynamics in red. The left plot depicts the scaling expected from Chini et al. (2022) with the perturbations decaying with $Fr^{1/2}$. The right plot shows the perturbations scaling with $(Fr^2/Pe)^{1/6}$ as predicted by Shah et al. (2023)

various regimes of stratified turbulence. A regime diagram depicting the dynamics of stratified turbulence within the (Pe, Fr) parameter space, taken from Shah et al. (2023), is shown in Figure 7, for $Pr = 0.1$ and $Pr \simeq 0.0002$, showing the unstratified region in gray, the viscous regime ($Re_b \leq 1$) in white, the non-diffusive regime in green, and the intermittent ($Fr \ll Pe_b \ll 1$) and thermally-diffusive ($Pe_b \ll Fr$) regimes in yellow and purple, respectively.

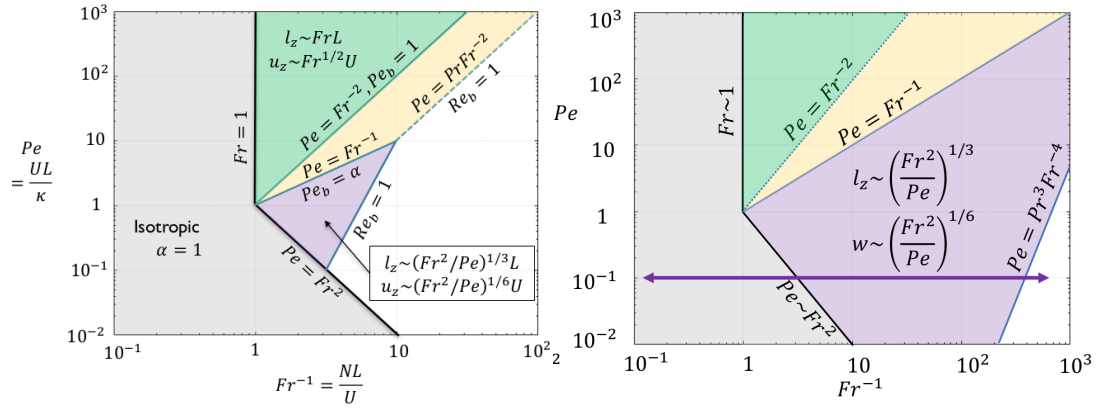

Figure 7: Flow regime diagram in Péclet/Froude parameter space at $Pr = 0.1$ (left) and at $Pr = 0.00017$ (right) taken from Garaud et al. (2024).

4 Stochastically forced non-rotating DNS

As discussed in Section 2, we implemented a stochastic forcing in the governing equations in preparation for running DNS of rotating stratified turbulence. The Coriolis force has a tendency to create steady span-wise flows in the steadily forced simulations which are not particularly realistic. Instead, we prefer using stochastic forcing in order to maintain isotropy in the horizontal direction. This section compares the results of non-rotating DNS using this new forcing against those of Garaud (2020) and Garaud et al. (2024).

4.1 Numerical Model

The DNS are conducted using the same PADDI code as in Cope et al. (2020), Garaud (2020), and Garaud et al. (2024). We use a domain size of $(4\pi \times 4\pi \times \pi)$ as illustrated in Figure 1 and with $(256 \times 256 \times 64)$ Fourier modes in (x, y, z) respectively. Most simulations, unless specifically indicated otherwise, are run with $Re = 600$ and $Pr = 0.1$ (i.e. $Pe = 60$), as in Garaud (2020) and Garaud et al. (2024), and vary the Froude number.

DNS are initialized either from random initial conditions at $t = 0$, or, by restarting the simulation from a previous run at different input parameters. In the first scenario, the initial conditions are:

$$\begin{cases} \boldsymbol{u}_h(\boldsymbol{x}, 0) = 0, \\ w(\boldsymbol{x}, 0) = \epsilon(\boldsymbol{x}), \\ T(\boldsymbol{x}, 0) = \epsilon(\boldsymbol{x}) \end{cases} \tag{4.1}$$

where $0 < |\epsilon(\boldsymbol{x})| \ll 1$ is a small amplitude random white noise. A divergence-cleaning operator is then applied to ensure that $\nabla \cdot \boldsymbol{u} = 0$ at $t = 0$. By forcing only the horizontal component of the momentum equation, the simulations rely on some form of instability to transfer energy into the vertical component of velocity, rather than forcing the vertical component of velocity directly. In the second scenario, simulations are restarted from a prior simulation with a change in one of the relevant parameters such as the Froude number (or Rossby number for the rotating runs). In both cases, simulations exhibit a transient phase known as the "spin-up" before the flow adjusts to become statistically stationary. For DNS started from (4.1), the horizontal components of

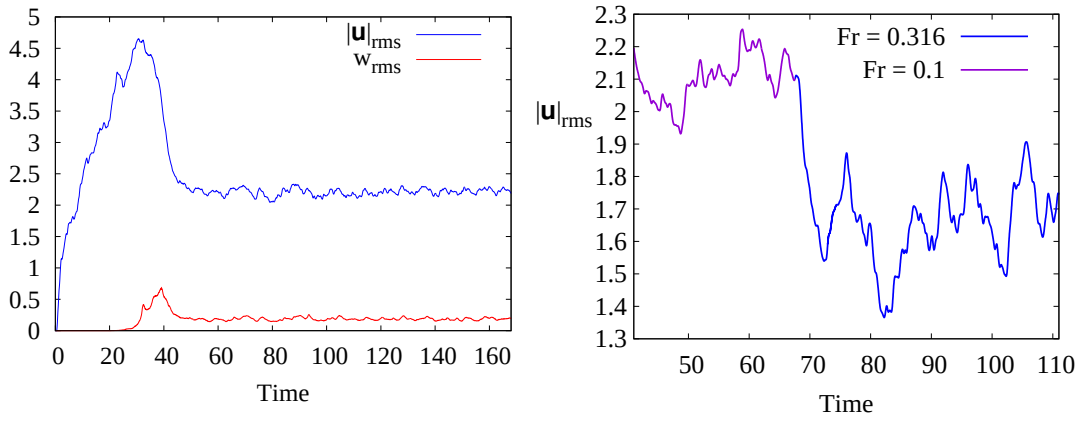

Figure 8: Timeseries of the root-mean-squared total velocity $\boldsymbol{u}_{\rm rms}$ and vertical velocity $w_{\rm rms}$ obtained from a non-rotating DNS with $Fr = 0.1$, $Re = 600$, $Pr = 0.1$ (left), and a time series of $\boldsymbol{u}_{\rm rms}$ during the transient phase from $Fr = 0.1$ to $Fr = 0.32$ at $Re = 1000$.

the velocity grow quickly in response to the forcing and begin to generate horizontal shear. The shear drives an instability, allowing the perturbation in the vertical velocity to exponentially grow to $O(1)$ as seen in Figure 8. The horizontal velocity then decays again as the instability settles into a statistically steady state. Typically, this transient phase lasts about 50 time units. For simulations restarted with a parameter change, the transient phase is typically shorter, and results in adjustments to the rms velocities and changes in the flow structure, see the right panel of Figure 8.

4.2 Typical Non-Rotating Simulations

Once in a statistically steady state, the flow structures that emerge are qualitatively similar to those observed by Cope et al. (2020) and Garaud et al. (2024). The horizontal flow field u forms layers on short vertical length scales, which are seen in Figure 9 to decrease with the Froude number. For stronger stratifications, the flow becomes more laminar while the turbulence is confined to localized patches, as discussed by Garaud et al. (2024).

Inspecting the vertical velocities at the same instants in time (see Figure 10) reveals that the vertical velocity is strongest within these turbulent regions.

The horizontal spectra seen in Figure 11 confirm that the larger-scale mean flow is anisotropic and dominated by mostly horizontal energy. The flow becomes isotropic at a wavenumber which becomes larger as the Froude number decreases. Note the transition from a $|k_h|^{-3}$ spectrum to a

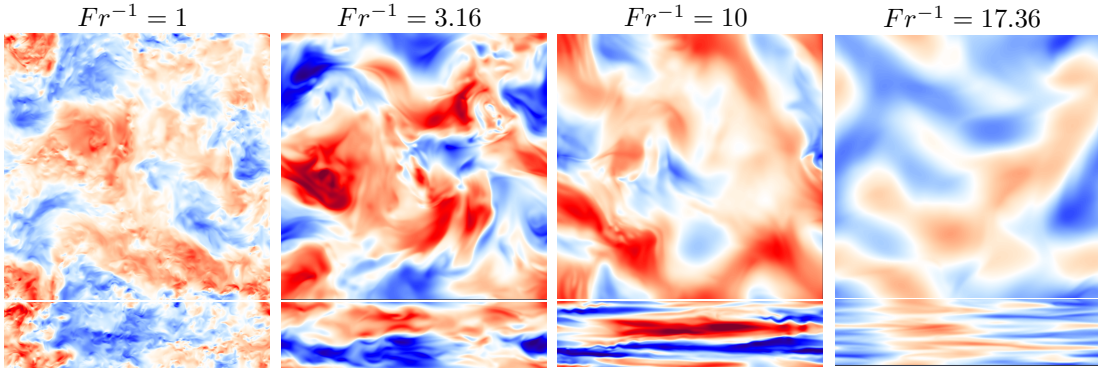

Figure 9: Snapshots of u on a horizontal slice through the top of the domain (top row) and on a vertical slice through the side of the domain (bottom row), for DNS at $Re = 600$, $Pr = 0.1$ and stratification increasing from left to right. The snapshot of the flow is taken from a statistically stationary state.

$|k_h|^{-5/3}$ spectrum as the flow becomes isotropic. Finally, at larger wavenumbers the flow become viscously dominated and no longer follows the $|k_h|^{-5/3}$ scaling. Our results are quite similar to the horizontal spectra presented by Garaud et al. (2024), with the exception of the plateau of the horizontal energy at small wavenumbers. That is explained by the forcing mechanism used, which in these simulations provides a similar amount of energy to wavenumbers below $|k_h| < \sqrt{2}$. By contrast, Garaud et al. (2024) used a forcing which excited only the smallest non-zero horizontal wavenumber, so the plateau is absent in their spectra.

In summary, we appear to be observing the same phenomena in these simulations that have been seen in prior work, at least from a qualitative point of view, with some minor discrepancies that can be explained by the forcing employed here.

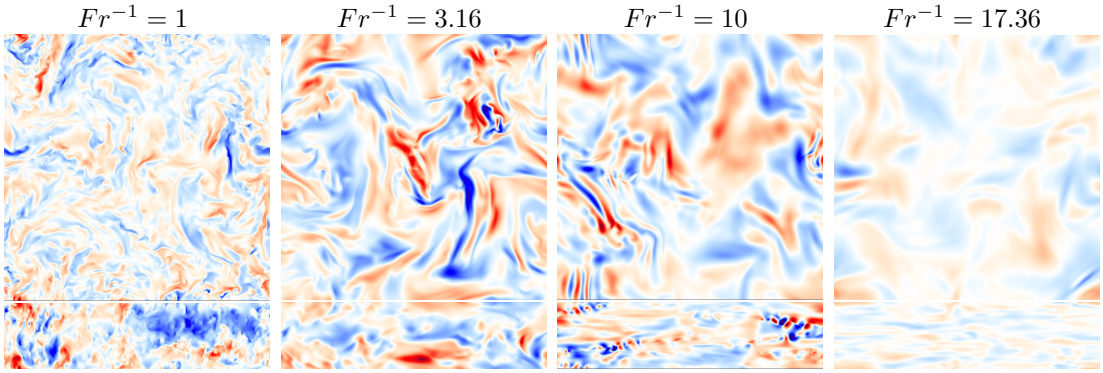

Figure 10: Snapshots of w on a horizontal slice through the top of the domain (top row) and on a vertical slice through the side of the domain (bottom row), for the same simulations and times as in Figure 9.

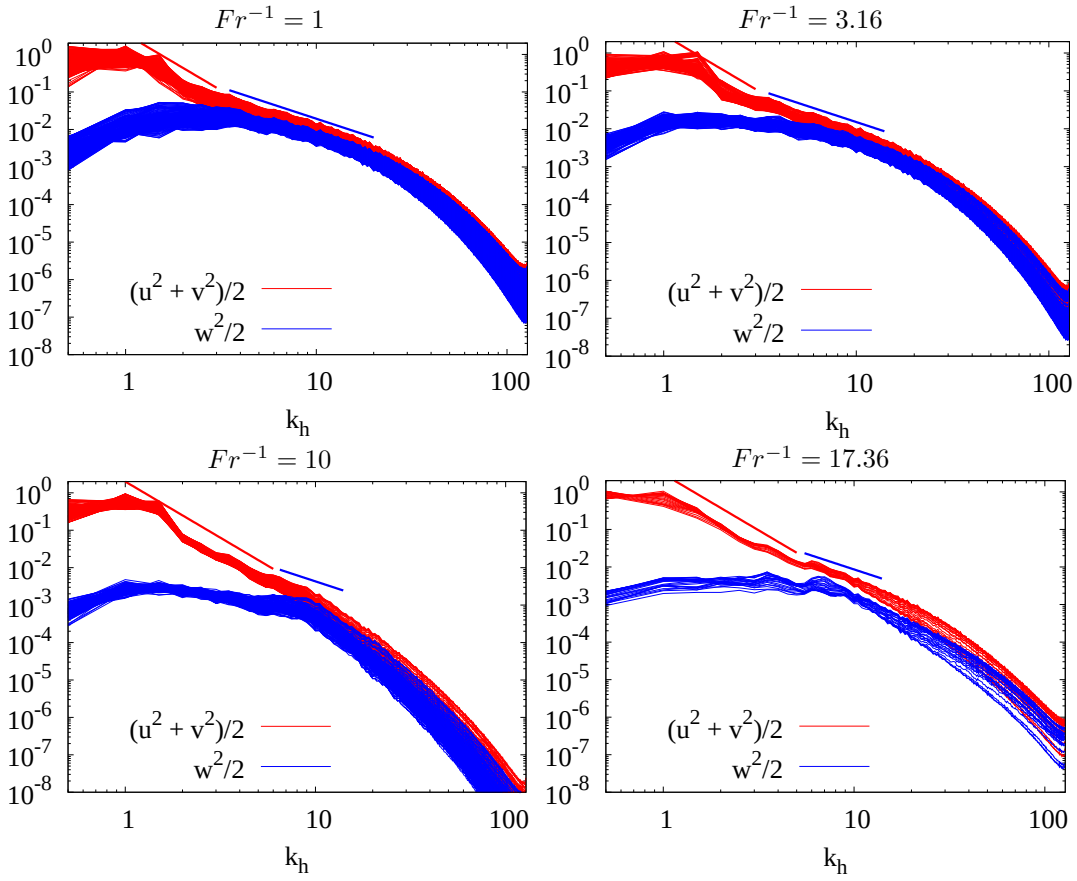

Figure 11: Kinetic energy spectra for the horizontal flow (red) and vertical flow (blue), as a function of the horizontal wavenumber k_h, for a range of Froude numbers. Overplotted in each panel is a red line showing a k_h^{-3}scaling law, and a blue line showing a $k_h^{-5/3}$ scaling law. Note the plateau in the horizontal energy for wavenumbers below ~ 1.5, corresponding to the stochastically forced range.

4.3 Quantititative Analysis

We now extract the rms vertical velocity from the data to see if it follows the scaling laws first presented by Chini et al. (2022) and then numerically validated by Garaud et al. (2024). Because of the spatiotemporal intermittency of the turbulence observed at larger stratifications, we employ the same vorticity-weighted rms velocities (3.18) and (3.19) used by Garaud et al. (2024) in order to isolate mean (large scale, slow) and perturbation (small scale, fast) dynamics. The results are presented in Figure 12, which shows $w_{\rm turb}$ in blue and $w_{\rm lam}$ in red, for various simulations. The steadily forced $Re = 600$ DNS data from Garaud et al. (2024) is plotted alongside the data from our DNS (see legend for detail). Overall, we see that these characteristic

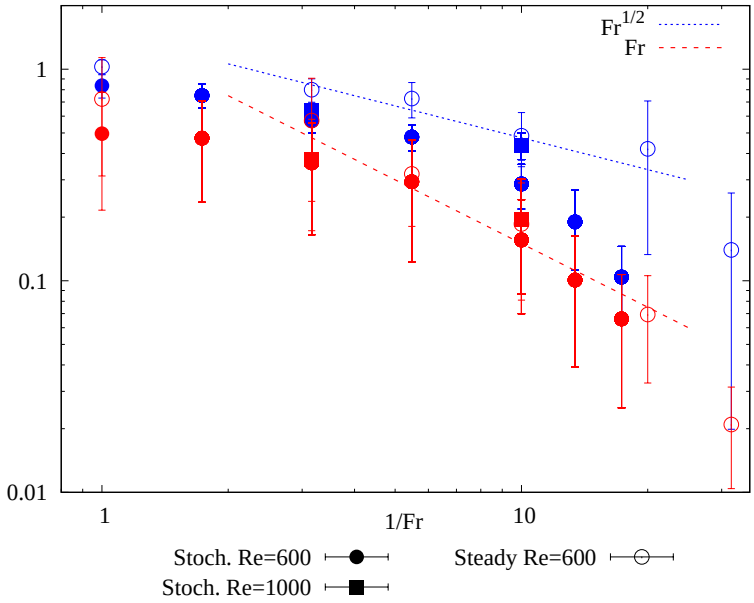

Figure 12: Weighted rms velocities $w_{\rm turb}$ (blue) and $w_{\rm lam}$ (red) as a function of $1/Fr$, for various simulations. Filled symbols correspond to the new data from stochastically-forced simulations, while open symbols correspond to the data of Garaud et al. (2024).

vertical velocities decrease with increasing stratification as expected. Furthermore, we find that the measurements of $w_{\rm lam}$ are similar between the two types of forcing, and follow the predicted scaling of $w_{\rm lam} \propto Fr$ (Chini et al., 2022) for sufficiently strong stratification. However, we also find that $w_{\rm turb}$ is systematically smaller in the stochastically forced simulations than in the steadily-forced simulations, and seems to decay faster with increasing stratification than the predicted $Fr^{1/2}$ scaling law.

To understand why that might be the case, we ran 2 additional simulations with $Re = 1000$ and $Pr = 0.1$. These data points are shown as squares in Figure 12 and seem to be more consistent with the steadily forced DNS at $Re = 600$. Furthermore, the difference between $w_{\rm turb}$ measured in the $Re = 600$ and $Re = 1000$ simulations for $Fr = 0.1$ shows that the $Re = 600$ run is actually partially viscously influenced. This implies that the simulations with $Fr < 0.1$ are also viscously influenced, and explains why they do not follow the $Fr^{1/2}$ scaling law for $w_{\rm turb}$. This result is consistent with our inspection of the horizontal energy spectrum for $Fr \leq 0.1$ in Figure 11.

We also present the mixing efficiency given by (2.17) as a function of the stratification in Figure 13, comparing again the stochastically-forced simulations with those of Garaud (2020) and

Garaud et al. (2024). The qualitative behavior appears to be similar between the two sets of data. We see a gradual increase of the mixing efficiency at lower values of $1/Fr$, which reaches a plateau at intermediate stratifications (corresponding to the strongly stratified turbulent regime), and then decays as the flow becomes viscously influenced at higher $1/Fr$ values. We observe the same trend in both sets of DNS, whereby η decays more rapidly with increasing stratification in lower Re simulations than in higher Re simulations, suggesting that these flows have started to become viscous earlier than their high Re counterparts. This is as expected. Despite these similarities, there is also a crucial difference between the sets of simulations. The stochastic forcing seems to generate flows with a mixing efficiency that peaks at $\eta \approx 0.5$ for intermediate stratification. This differs from the prior DNS with the steady shear forcing which sees the mixing efficiency peak at $\eta \approx 0.4$ and implies that the mixing might be caused by different instabilities altogether.

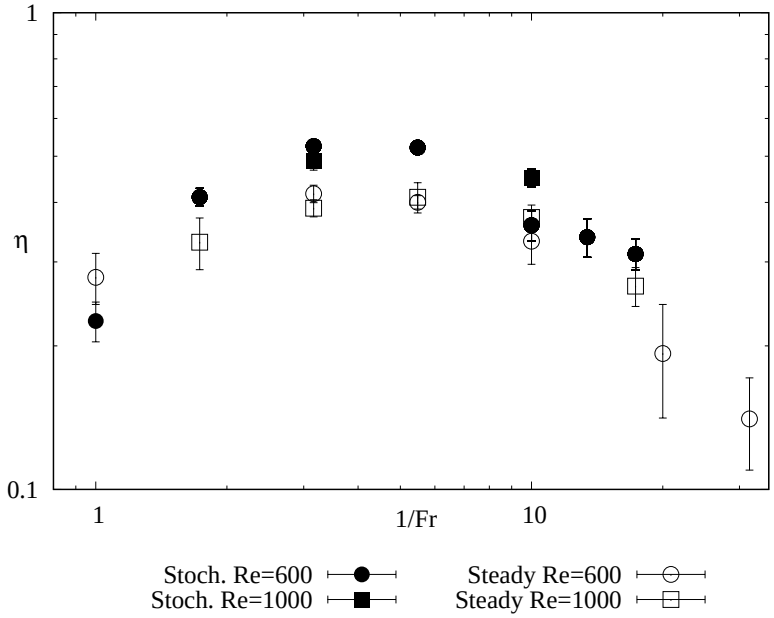

Figure 13: Mixing efficiency η defined in (2.17) as a function of $1/Fr$.

We believe that several factors may contribute to the aforementioned differences between the new stochastically-forced simulations and the previous DNS with steady forcing. One such factor is the difference in the effective non-dimensional parameters of the flow. The non-dimensionalization selected assumes that the characteristic horizontal scale of the eddies is 1. In previous DNS with steady forcing, Garaud (2020) and Garaud et al. (2024) selected their

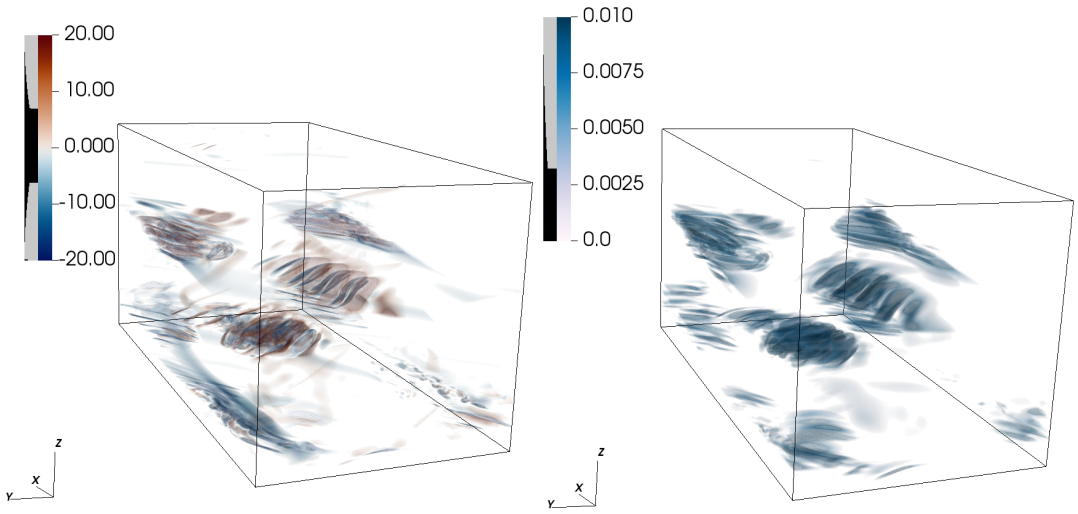

Figure 14: Volume rendering of the vertical vorticity ω_z (left) and χ (right) taken from a steady-forcing DNS by Garaud (2020) with $Re = 600$, $Pr = 0.1$ and $Fr = 0.05$. The figure demonstrates a strong correlation between the regions of strong vertical vorticity and strong thermal dissipation.

forcing wavenumber to be 1, accordingly. In our DNS, however, wavenumbers up to $|\boldsymbol{k}_h| = \sqrt{2}$ are forced so the characteristic length scale of the eddies is correspondingly smaller than in equivalent steady-forced simulations by a factor of $\sqrt{2}$. This suggests that the input Reynolds number Re of the stochastically forced simulations probably ought to be scaled by a factor of $1/\sqrt{2}$ for a more meaningful comparison with the steady-forced simulations, i.e. $Re = 600$ in our simulations corresponds to $Re_{\text{Eff}} \approx 424$ in the simulations by Garaud (2020) and Garaud et al. (2024). This could explain why our simulations appear to become viscous at weaker stratifications compared to prior DNS.

Beyond superficial differences in the non-dimensionalization, there also appear to be more fundamental differences in the flow dynamics. In particular, we believe that there is a new mechanism for generating small horizontal length scales in the stochastically forced flow that is not present in simulations with steady forcing. In the steadily forced DNS (and in the multiscale theory by Chini et al. (2022)), small horizontal length scales can only be generated by the vertical shear instability and are, therefore, indicative of buoyancy mixing events. The stochastic forcing, by contrast, seems to produce small horizontal scales that are not associated with mixing events.

We demonstrate this in Figures 14 and 15 using the thermal dissipation rate $\chi = \langle |\nabla T|^2 \rangle / Pe$, a strong indicator of mixing events, and the vertical vorticity ω_z, a quantity that is strongest in

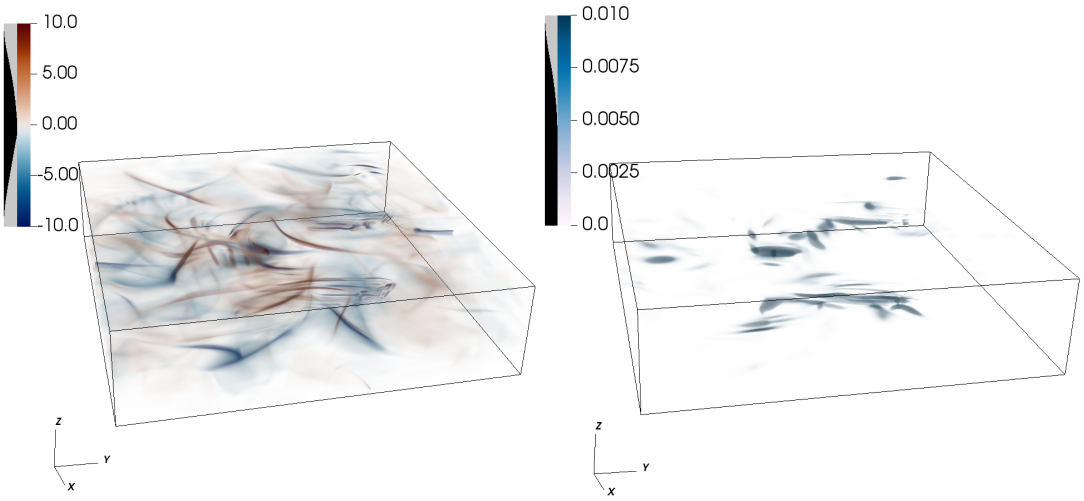

Figure 15: Volume rendering of the vertical vorticity ω_z (left) and $|\nabla T|^2/Pe$ (right) taken from a stochastically-forced simulation at $Re = 600$, $Pr = 0.1$ and $Fr = 0.074$ simulation. Regions of strong vertical vorticity and strong thermal dissipation are not as clearly correlated.

flows with small horizontal length scales. Figure 14 presents a volume rendering of both ω_z and χ at the same time from a strongly-stratified simulation taken from Garaud (2020). We observe a strong correlation between the regions where the thermal dissipation is strongest and the regions where the vertical vorticity is also strongest, suggesting that small horizontal scales are always associated with instabilities that mix buoyancy. Figure 15, by contrast, presents similar volume renderings of ω_z and χ in stochastically-forced DNS and shows that the correlation is this time not as strong. While some of the high $|\omega_z|$ regions also have high χ, there are several structures in the vertical vorticity, however, which do not appear to have a visible counterpart in the thermal dissipation. We conclude then that there must be some mechanism to generate these scall horizontal scales besides the vertical shear instability. We hypothesize that these are caused by the advection of the mean horizontal flow by the stochastically forced vortices, which can cause some filamentation and, thus, the emergence of small horizontal scales not associated with vertical mixing.

The appearance of small non-turbulent horizontal scales has another important consequence. Garaud et al. (2024) used the magnitude of the vertical vorticity as a diagnostic to isolate turbulent patches. Since the vertical vorticity is no longer exclusively strong in regions of strong mixing events, the algorithms to generate $w_{\rm turb}$ (3.18) and $w_{\rm lam}$ (3.19) are no longer effective at isolating perturbation dynamics from the mean flow dynamics. As a result, in what follows we

shall solely use w_{rms} to measure the effect of stratification/rotation on vertical mixing.

In conclusion, the stochastic forcing used here produces flows that exhibit the general behavior expected of stratified turbulence. However, the flow structure is distinct from prior work which used a steady forcing in as much as it leads to the generation of small horizontal scales that are not necessarily related to vertical mixing processes.

5 Rotating Stratified Turbulence

5.1 Model setup

We now explore the effects of rotation on the stochastically-forced stratified turbulence simulations. The DNS presented in this section have the same setup as the DNS in §2.5 with the inclusion of the Coriolis term in the momentum equation (2.4) encoded into PADDI. Simulations are presented here for two different Froude numbers in the strongly stratified regime, and vary the Rossby number.

5.2 Typical Simulations

We begin by presenting simulations with $Fr = 0.18$, $Re = 600$, $Pr = 0.1$ and gradually increase the rotation rate. Snapshots of the simulations in a statistically stationary state are presented in Figures 16 and 17 for u and w respectively.

Rotation begins to influence the flow dynamics as the Rossby number decreases below 1, as expected. Indeed, in Figure 16, we see the appearance of columnar vortices in the horizontal velocity field for $Ro^{-1} \geq 1$. Inspecting these vortices reveals that they span the entire vertical extent of the domain, a phenomenon known generally as "Taylor Columns". These columns seem to become more vertically invariant as the rotation rate increases. Outside of these columns, the flow continues to have small vertical scales. Furthermore, as the Rossby number decreases, the horizontal scale of columns approaches the size of the domain, and the characteristic horizontal velocities increase despite the fact that the forcing remains the same. This is suggestive of an inverse cascade to large scales, leading to the formation of a so-called "condensate".

From Figure 17, we see that the vertical velocity is also affected by the appearance of the Taylor columns in the flow. In fact, we see that the small vertical length scales are increasingly suppressed within the columns as the Rossby number decreases. Furthermore, the magnitude of the vertical velocity becomes weaker within the columns. Instead, vertical mixing events appear to be localized outside of the columns.

To gain more insight into the flow structure, and in particular, the anti-correlation between the Taylor columns and the regions of strong mixing, we now present volume renderings of the DNS in Figure 18. On the left, we show the vertical vorticity ω_z, and on the right, we show the local thermal dissipation rate $|\nabla T|^2/Pe$, which is a measure of irreversible mixing.

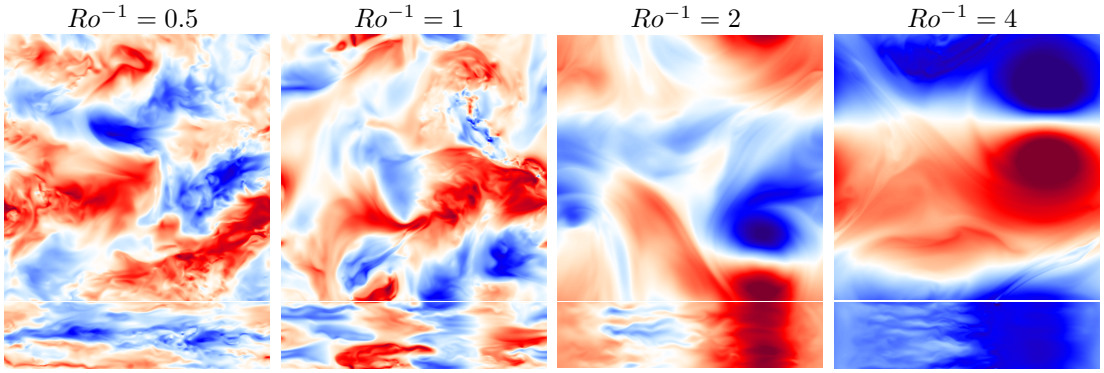

Figure 16: Instantaneous snapshots of u on a horizontal slice through the top of the domain (top row) and on a vertical slice through the side of the domain (bottom row). In all cases, $Re = 600$, $Pr = 0.1$, $Fr = 0.18$. For lower Rossby DNS, Taylor columns spontaneously emerge from the flow and begin to dominate the flow dynamics.

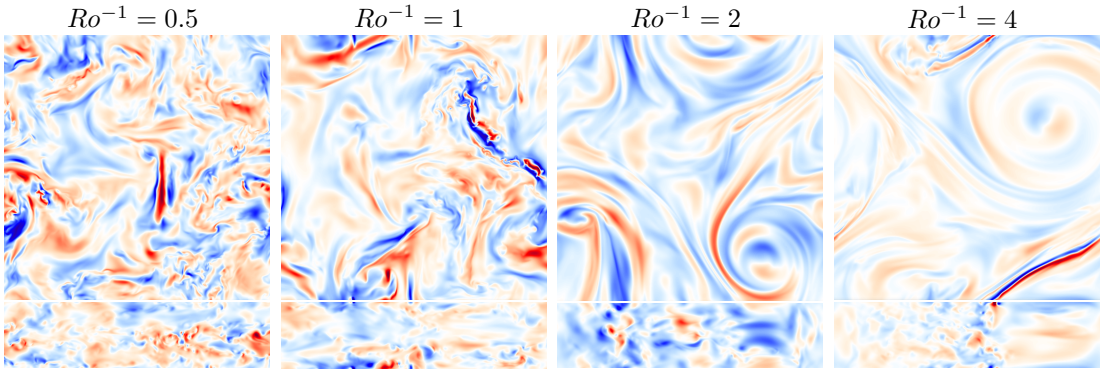

Figure 17: Instantaneous snapshots of w on a horizontal slice through the top of the domain (top row) and on a vertical slice through the side of the domain (bottom row). The snapshots are taken at the same time as in Figure 16. The Taylor columns are also visible in the vertical velocity field, corresponding to regions of large-scale, low w.

For weak rotation rates (top row), there is no evidence of columnar structure and both ω_z and $|\nabla T|^2/Pe$ seem to be distributed evenly throughout the domain. As the rotation rate increases (middle row), we see the appearance of vertically invariant, cyclonic vortices, which correspond to regions where mixing is strongly suppressed. The anti-cyclones, on the other hand, remain more turbulent and correspond to regions of strong mixing. As Ω/N approaches 1, or equivalently as Ro approaches $Fr/2$, the anti-cyclones become rotationally constrained as well (bottom row), suggesting that mixing might become fully suppressed for $Ro \ll Fr/2$.

Figure 19 shows plots of the horizontal and vertical kinetic energy spectrum for these simulations as well as additional ones for larger rotation rates. Inspection of the horizontal energy spectrum confirms that there is indeed an inverse cascade of energy, most clearly visible for

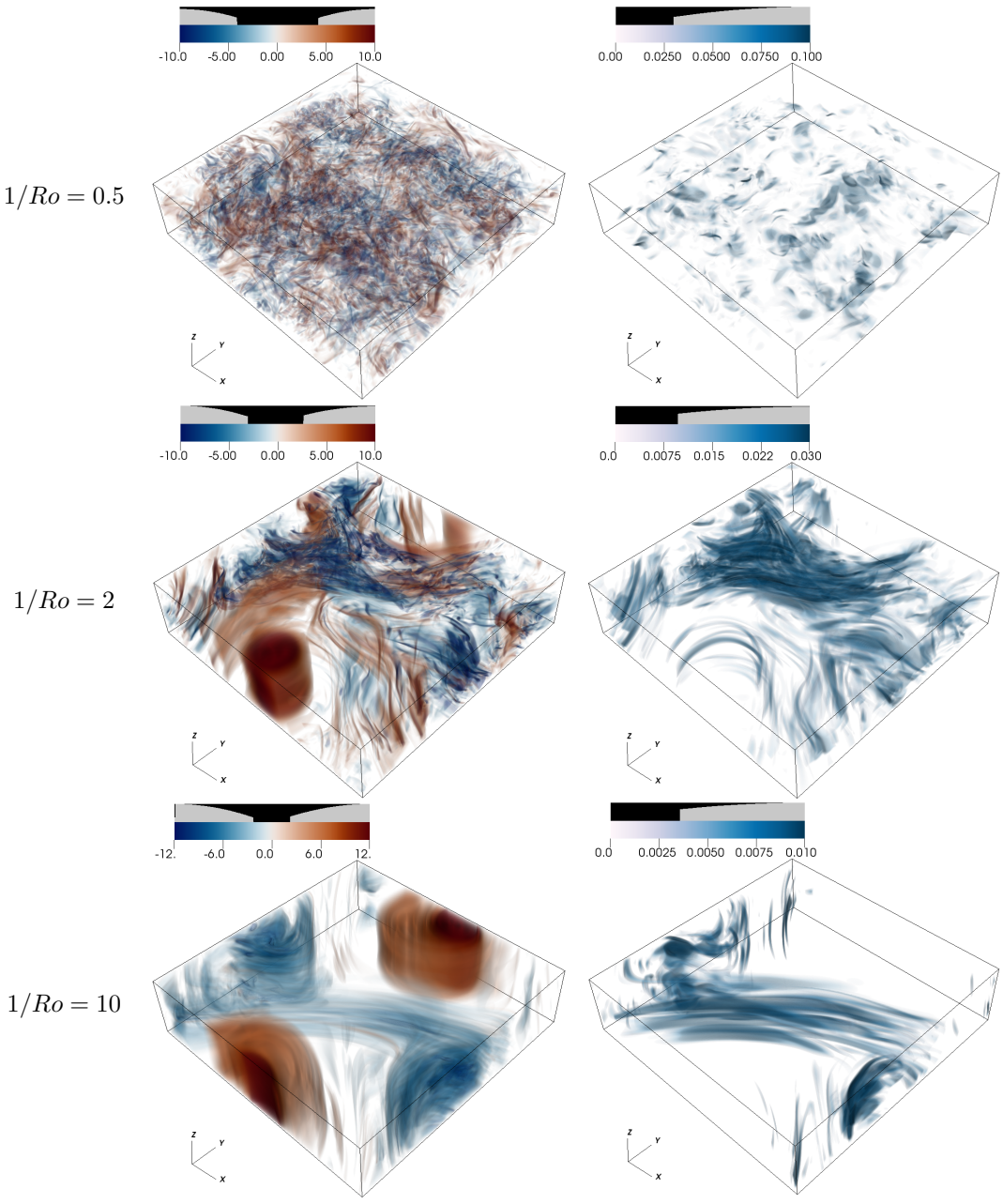

Figure 18: Volume rendering of the vertical vorticity ω_z (left) and of the local thermal dissipation $|\nabla T|^2/Pe$ (right) from DNS with $1/Ro = 0.5$ (top), $1/Ro = 2$ (middle), and $1/Ro = 10$ (bottom), for $Re = 600$, $Pr = 0.1$ and $Fr = 0.18$.

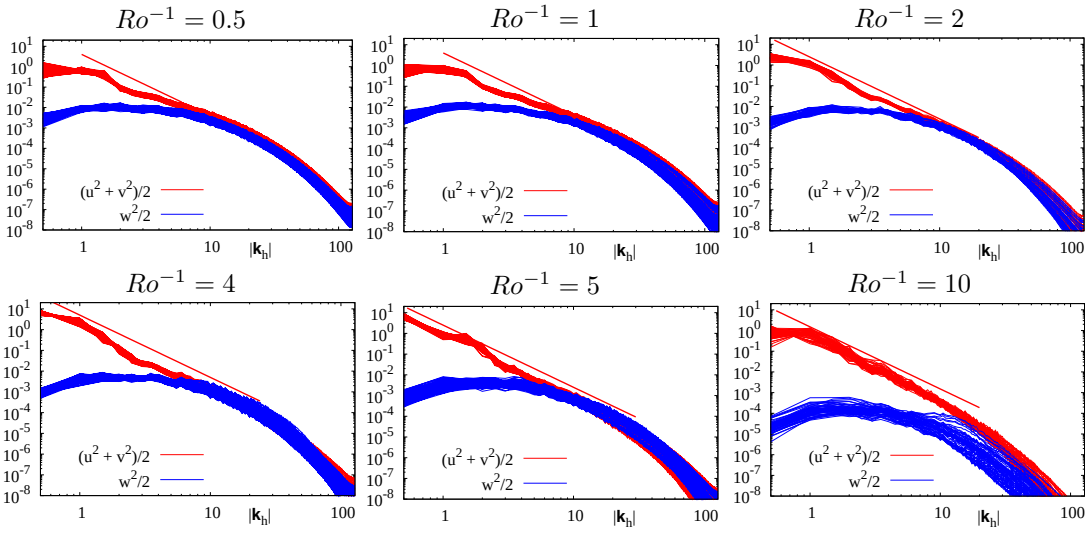

Figure 19: Energy Spectrum of the flow according to the total horizontal wavenumber $|k_h|$ for flows with varying Rossby numbers (decreasing from left to right, then top to bottom). The red lines represent the total horizontal energy $(u^2+v^2)/2$ at different time steps while the blue lines represent the vertical energy $v^2/2$. As the rotation rate increases, we see an inverse cascade of energy transferring energy into the smallest wavenumbers in the domain. Furthermore, the vertical energy decreases with the Rossby number achieving a lower maximum in smaller Rossby number simulations. Finally, the energy spectra follow the $|k_h|^{-3}$ scaling to larger wavenumbers as the Rossby number becomes smaller.

$1/Ro \geq 4$, piling large amounts of energy at the smallest horizontal wavenumber in the domain. The horizontal kinetic energy spectrum appears to follow the $|k_h|^{-3}$ law at small wavenumbers, as before, and we can see that it continues to follow this scaling even after the flow becomes isotropic at larger wavenumber (at least for $Ro^{-1} \geq 4$). In addition, the vertical kinetic energy spectrum seems to have a lower maximum value with decreasing Rossby number, with the typical vertical energy at $1/Ro = 10$ being roughly a factor of 10 less than for $1/Ro = 0.5$.

An important caveat of these conclusions is that the lowest Rossby number simulations may not have reached a sufficiently long period in a statistically stationary state. This is because the timestep needs to be very small in simulations with higher rotation rates. Due to the Courant condition, we must have $\Delta t \leq \Delta x/U_{\max}$, where Δx is the grid resolution, and $U_{\max}$ is the maximum velocity in the domain at any given moment. As the Rossby number decreases and more energy is transferred into horizontal motions, $U_{\max}$ increases, and therefore, the number of timesteps needed to achieve the same simulation time increases as well. Due to this, our lowest Rossby number simulations are not fully integrated into a statistically stationary state.

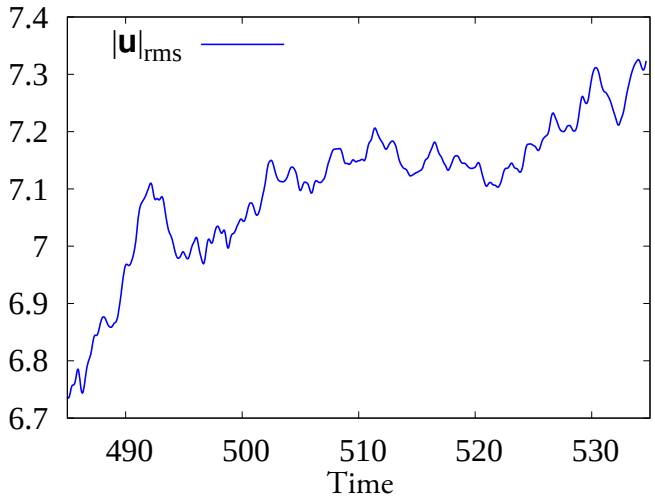

Figure 20: Time series of $|\boldsymbol{u}|_{\text{rms}}$ in a DNS with $Re = 600$, $Pr = 0.1$, $Fr = 0.18$ and $Ro = 0.1$. The time series generated is shorter, and yet cost the same amount of compute time as the time series shown in Figure 8.

Simulations that have not reached a statistically stationary state will be labeled differently in the next section.

5.3 Quantitive Analysis

We now investigate the effect of rotation on more quantitative aspects of stratified turbulence. Figure 21 presents plots of the horizontal and vertical velocities, of the mixing efficiency, and of the temperature flux as functions of the rotation rate (measured by $1/Ro$). Two sets of DNS are shown, a series with Froude number $Fr = 0.18$ corresponding to a more weakly stratified system in blue and a series with $Fr = 0.1$ corresponding to a more strongly stratified system in red. In each plot, the vertical dotted line represents the value $1/Fr$ for each Froude number respectively.

As expected from the DNS visualizations presented in the previous section, we find that the rms horizontal velocity increases as the Rossby number decreases below 1. By contrast, proxies for vertical mixing (vertical temperature flux, mixing efficiency, and vertical velocity) are roughly constant, until Ro approaches Fr. For Rossby number smaller or equal to Fr we see that mixing is strongly suppressed. We hypothesize that this is because the Taylor columns take up larger fractions of the domain, inhibiting vertical mixing as the Rossby number decreases past Fr.

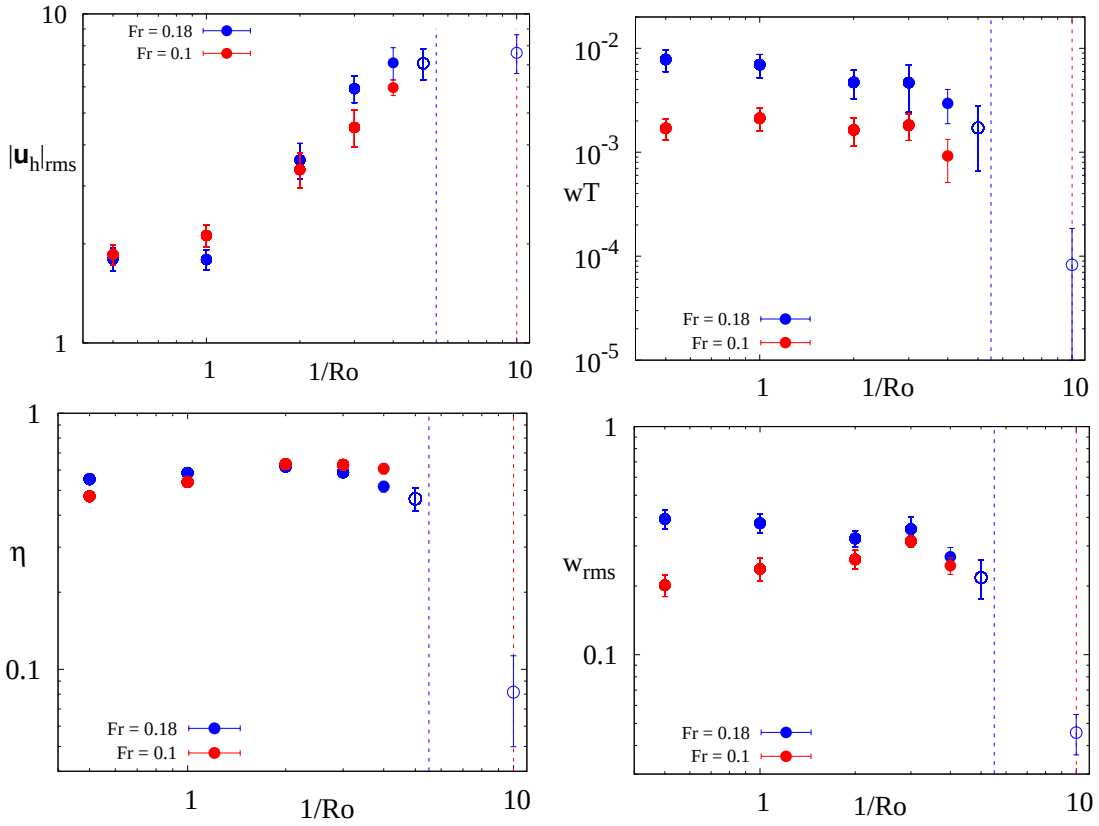

Figure 21: Measurements from DNS with varying Rossby number. Points shown in blue are of a series of DNS with $Fr = 0.18$ and those in red are taken from DNS with $Fr = 0.1$. In all cases, $Re = 600$ and $Pr = 0.1$. The open circles indicate DNS that have not reached a statistically stationary state yet. The top left panel shows the horizontal rms velocity $|\boldsymbol{u}_h|_{\mathrm{rms}}$, the top right shows the temperature flux $\langle wT \rangle$, the bottom left is the mixing efficiency η, and the bottom right is the vertical rms velocity w_{rms}.

5.4 Insight from Multiscale Analysis

In order to explain the DNS results, we return to the multiscale analysis presented by Chini et al. (2022) and introduce the Coriolis term to the horizontal momentum equations (3.7), (3.8). The mean and perturbation equations become

$$\begin{aligned} &\frac{\partial \bar{\boldsymbol{u}}_h}{\partial t_s} + \bar{\boldsymbol{u}}_h \cdot \nabla_s \bar{\boldsymbol{u}}_h + \frac{1}{\alpha}\overline{\boldsymbol{u}_h' \cdot \nabla_f \boldsymbol{u}_h'} + \frac{\bar{w}}{\alpha}\frac{\partial \bar{\boldsymbol{u}}_h}{\partial \zeta} + \overline{\frac{w'}{\alpha}\frac{\partial \boldsymbol{u}_h'}{\partial \zeta}} + \frac{1}{Ro}\boldsymbol{e}_z \times \bar{\boldsymbol{u}}_h \\ &= -\nabla_s \bar{p} + \bar{\boldsymbol{F}}_h + \frac{1}{Re_b}\frac{\partial^2 \bar{\boldsymbol{u}}_h}{\partial \zeta^2} + h.o.t., \end{aligned} \tag{5.1}$$

$$\begin{aligned}&\frac{1}{\alpha}\frac{\partial \boldsymbol{u}_h'}{\partial t_f}+\frac{1}{\alpha}\bar{\boldsymbol{u}}_h\cdot\nabla_f\boldsymbol{u}_h'+\frac{w'}{\alpha}\frac{\partial\bar{\boldsymbol{u}}_h}{\partial\zeta}+\frac{1}{Ro}\boldsymbol{e}_z\times\boldsymbol{u}_h'\\&=-\frac{1}{\alpha}\nabla_f p'+\frac{1}{Re_b}\left(\nabla_f^2\boldsymbol{u}_h'+\frac{\partial^2\boldsymbol{u}_h'}{\partial\zeta^2}\right)+h.o.t.\ .\end{aligned}\tag{5.2}$$

We see from equation (5.1) that we should expect rotation to affect the mean flow when $1/Ro$ becomes $O(1)$, and that the effect of rotation on $\bar{\boldsymbol{u}}_h$ should become dominant when $Ro \ll 1$. When $Ro = O(1)$, by contrast, we see from equation (5.2) that the perturbations to the mean flow are unaffected by rotation, as the crucial ratio α/Ro is still very small (recall that $\alpha \ll O(1)$). It is only when Ro approaches α that we expect the perturbations to start feeling the effects of rotation, and when $Ro \ll \alpha$ that rotation will dominate the perturbation dynamics. We, therefore, expect (at least) three regimes: $Ro \geq O(1)$ where rotation is not dominant, $\alpha \leq Ro \ll 1$ where rotation dominates the mean but not the fluctuations, and $Ro \ll \alpha$ where rotation dominates at all scales.

When $\alpha \ll Ro \ll 1$, we expect columns to develop in the mean flow as the mean equations become geostrophically balanced, i.e.

$$\frac{1}{Ro}\boldsymbol{e}_z\times\bar{\boldsymbol{u}}=-\nabla_s\bar{p},\tag{5.3}$$

where we must have $\bar{p} = O(Ro^{-1})$ in order to balance the horizontal momentum equation. Because the other equations of motion are unaffected by rotation, we still have that $\bar{T}, \bar{w} \leq O(\alpha)$. Therefore, the leading order of the vertical momentum equation (3.11) becomes

$$\frac{1}{\alpha}\frac{\partial\bar{p}}{\partial\zeta}=0\ ,\tag{5.4}$$

and we have that $\nabla_s\bar{p} = \nabla\bar{p}$ to leading order. In order to show that the mean flow becomes vertically invariant, we take the curl of equation (5.3) and find that $\frac{\partial\bar{\boldsymbol{u}}}{\partial\zeta} = 0$ to leading order. For this reason, we see the appearance of columns in the flow which seem to dominate the mean dynamics but which do not completely suppress mixing and vertical transport.

If we suppose that the Rossby number were to become smaller than α which is the case for $Ro < Fr$ (still assuming that $\alpha = Fr$), the leading order of the horizontal momentum equations

now becomes,

$$\frac{1}{Ro}\boldsymbol{e}_z \times \bar{\boldsymbol{u}}_h = -\nabla_s \bar{p}, \tag{5.5}$$

$$\frac{\alpha}{Ro}\boldsymbol{e}_z \times \boldsymbol{u}'_h = -\nabla_f p'. \tag{5.6}$$

In this limit, the perturbations also become vertically invariant for similar reasons, and mixing in the flow is heavily suppressed. With the limited data presented in Figure 21, it is clear that the $Fr = 0.18$ simulations experience this transition, evinced by the proxies of mixing declining quickly after passing the threshold value.

6 Discussion and Conclusion

In this work, we have studied rotating stochastically-forced stratified turbulence using direct numerical simulations. In the non-rotating case, we have shown that stochastically forced stratified turbulence exhibits subtle differences in flow properties compared to steadily forced DNS. The mixing efficiency is notably larger in the stochastically forced case, and regions of high vertical vorticity are not always correlated with strong mixing events. Specifically, small horizontal scales are produced in the stochastically forced flow, seemingly independent of an instability mechanism. As a result, we find that the method posited by Garaud et al. (2024) to isolate mean flow and perturbations by the vertical vorticity is not as relevant here, and probably ought to be replaced by an algorithm which uses the thermal dissipation as a weight function.

Our DNS of rotating stratified turbulence with $Fr \ll Ro \leq 1$ revealed strong columnar vortices in the mean flow structure. These vortices are primarily cyclonic and vertically invariant, thereby suppressing vertical mixing within their core. The flow also generates unstable anticyclonic regions, within which mixing still occurs. For very rapid rotation $Ro \ll Fr$, we find that vertical mixing is suppressed entirely and the flow becomes almost two-dimensional.

These preliminary results suggest opportunities to expand on the work presented here to resolve some outstanding issues. Foremost, the range of each dimensionless number Ro, Fr, Re investigated here needs to be expanded to cover parameter space more comprehensively. Furthermore, a small portion of the simulation data presented had not reached a sufficiently stationary state, and so these simulations need to be extended to confirm these results. We also acknowl-

edge that the effect of rotation is only investigated here at the poles of rotating bodies (i.e. where $\boldsymbol{e}_{\boldsymbol{\Omega}} = \boldsymbol{e}_z$). Rotation, as well as the β-effect, may influence the large-scale flow structure in different ways when rotation is not aligned with gravity. In order to generalize these results, one might need to run simulations in a spherical shell. Finally, we believe the multiscale theory for stratified turbulence developed by Chini et al. (2022) requires an additional vertical length scale in order to capture the dynamics within the columns that appear in the flow. As a consequence, we suspect that the value for α may indeed vary with the Rossby number in the rapidly rotating limit.

Despite these caveats, we find, as in Praud et al. (2006) and Aubert et al. (2012), that Ω/N, rather than Ro, seems to be the correct bifurcation parameter for determining the effect of rotation on vertical mixing by stratified turbulence. This indicates that regions of rotating stratified turbulence with $Fr \ll Ro \ll 1$ can have large-scale flows that are rotationally influenced, and yet allow substantial vertical mixing. Crucially, this limit is relevant for geophysical and astrophysical systems such as the solar tachocline ($\Omega/N = O(10^{-3})$) and the Earth's oceans ($\Omega/N = O(10^{-2})$) for modeling vertical mixing. This suggests that the theory of Chini et al. (2022) still models vertical mixing in these regions even though they are rapidly rotating in the sense that their Rossby number is small (Tulekeyev et al., 2024).

References

Aerts, Conny, Mathis, Stéphane, & Rogers, Tamara M. 2019, ARAA, 57, 35

Alvelius, K. 1999, Physics of Fluids, 11, 7, 1880

Aubert, Oriane, Le Bars, Michael, Le Gal, Patrice, & Marcus, Philip S. 2012, Journal of Fluid Mechanics, 706, 34–45

Billant, P., & Chomaz, J.-M. 2000, Journal of Fluid Mechanics, 419, 65–91

Brethouwer, G., Billant, P., Lindborg, E., & Chomaz, J. M. 2007, Journal of Fluid Mechanics, 585, 343

Chini, Gregory P., Michel, Guillaume, Julien, Keith, Rocha, Cesar B., & Caulfield, Colm-cille P. 2022, Journal of Fluid Mechanics, 933, A22

Cope, Laura, Garaud, P., & Caulfield, C. P. 2020, Journal of Fluid Mechanics, 903, A1

Garaud, P. 2020, apj, 901, 2, 146

Garaud, Pascale, P., Chini Gregory, Kaasturi, Shah, & Caulfield, Colm-cille P. 2024, JFM Rapids

Haynes, P. H., McIntyre, M. E., Shepherd, T. G., Marks, C. J., & Shine, K. P. 1991, Journal of Atmospheric Sciences, 48, 4, 651

Herring, J. R., & Metais, O. 1989, Journal of Fluid Mechanics, 202, 97

Holford, Joanne M., & Linden, P.F. 1999, Dynamics of Atmospheres and Oceans, 30, 2, 173

Howland, Christopher J., Taylor, John R., & Caulfield, C. P. 2020, Journal of Fluid Mechanics, 898, A7

Lilly, D. K. 1983, Journal of Atmospheric Sciences, 40, 3, 749

Lindborg, E. 2006, Journal of Fluid Mechanics, 550, 207–242

Maffioli, A., Brethouwer, G., & Lindborg, E. 2016, Journal of Fluid Mechanics, 794, R3

Maffioli, A., & Davidson, P. A. 2016, Journal of Fluid Mechanics, 786, 210–233

Munk, Walter H. 1966, Deep Sea Research and Oceanographic Abstracts, 13, 4, 707

Park, Young-Gyu, Whitehead , J., & Gnanadesikan, Anand 1994, Journal of Fluid Mechanics, 279, 279

Pinsonneault, M. 1997, Annu. Rev. Astron. Astrophys., 35, 557

Praud, O., Sommeria, J., & Fincham, A. M. 2006, Journal of Fluid Mechanics, 547, 389–412

Shah, Kasturi, Chini, Gregory P., Caulfield, Colm-cille P., & Garaud, Pascale 2023, arXiv e-

prints, arXiv:2311.06424

Smith, Katherine M., Caulfield, C.P., & Taylor, J.R. 2021, Journal of Fluid Mechanics, 910, A42

Thompson, M. J., Toomre, J., Anderson, E. R., Antia, H. M., Berthomieu, G., Burtonclay, D., Chitre, S. M., Christensen-Dalsgaard, J., Corbard, T., De Rosa, M., Genovese, C. R., Gough, D. O., Haber, D. A., Harvey, J. W., Hill, F., Howe, R., Korzennik, S. G., Kosovichev, A. G., Leibacher, J. W., Pijpers, F. P., Provost, J., Rhodes, E. J., Jr., Schou, J., Sekii, T., Stark, P. B., & Wilson, P. R. 1996, Science, 272, 1300

Traxler, A., Garaud, P., & Stellmach, S. 2011, Astrophys. J., 728, 2, L29

Tulekeyev, A., Garaud, P., Idini, B., & Fortney, J. J. 2024, Constraints on the long-term existence of dilute cores in giant planets

Waite, Michael L., & Bartello, Peter 2004, Journal of Fluid Mechanics, 517, 281

Waite, Michael L., & Bartello, Peter 2006, Journal of Fluid Mechanics, 568, 89

Williams, Christopher, & Rasmussen, Carl 1995, in Advances in Neural Information Processing Systems, eds. D. Touretzky, M.C. Mozer, & M. Hasselmo (MIT Press), vol. 8

Yi, Young R., & Koseff, Jeffrey R. 2023, Phys. Rev. Fluids, 8, 084803